Bachelorarbeit
Zur Erlangung des akademischen Grades Bachelor of Science

Superconductivity in MgB_2 combining Eliashberg theory with density-functional theory based methods

eingereicht von: Marten Henrik Pretorius

Gutachter/innen: Prof. , Claudia Draxl
PD, Pasquale Pavone

Eingereicht am Institut für Physik der Humboldt-Universität zu Berlin am:

Abstract

The framework of Eliashberg theory and density-functional theory based methods provides us with an *ab initio* method to study superconductivity. While it is apparent that qualitative descriptions of superconductors are possible within this framework, it is not clear how accurate the prediction of critical temperature T_c can be as many studies tune the coulomb interaction to obtain the experimentally measured T_c. In this work, we present an *ab initio* study of superconductivity in MgB_2 combining fully anisotropic Eliashberg theory with density-functional and density-functional perturbation theory. We are able to validate the two gap structure of MgB_2, obtaining two clusters of gap values, one centered at 2.4 meV and the other at 6.5 meV. For the critical temperature T_c we obtain a T_c of 37 K, which is in excellent agreement with the experimental result. Our study also demonstrates that the combination of Eliashberg theory and density-functional theory based methods is capable of accurately predicting T_c so long as the phonon energies are in good agreement with experimental data.

Contents

Chapter 1

Introduction

A superconductor is a material with vanishing resistivity and strong or perfect diamagnetism (Meissner effect). Materials that can become superconducting have a critical temperature T_c at which they undergo a transition between their normal phase ($T > T_c$) into a superconducting phase ($T < T_c$) [1].

The unique properties of superconductors, mainly the zero resistivity, have made it possible to build powerful electromagnets and extremely sensitive measurement devices that have already revolutionized many fields, *e.g.*, medical imaging of body interiors and particle accelerators. Superconductors are also used for levitating trains and power cables without loss of energy.

The superconducting phase can be destroyed by a magnetic field or a current density above a critical magnetic field $\mathbf{H}_c$ or current density $\mathbf{J}_c$ [1]. For wider technical applications, it is important to find materials with a high T_c, $\mathbf{H}_c$, and $\mathbf{J}_c$ [2]. An important threshold is a critical temperature of 77 K, which is the boiling temperature of liquid N_2. A material with $T_c > 77\,\mathrm{K}$ would not have to be cooled below its T_c using expensive liquid He but could be cooled using the vastly available liquid N_2.

Superconductivity was first discovered in 1911 by Onnes [3]. In Onnes's work, it was shown that the resistance of Hg vanishes below 4.16 K. The special diamagnetic properties of superconductors where discovered in 1933 by Meissner and Ochsenfeld. They found perfect diamagnetism in superconducting Pb and Sn [4]. It took almost 50 years since the discovery of the phenomenon until, in 1957, Bardeen, Cooper, and Schrieffer (BCS) presented a first theoretical framework for the phenomenon known as the BCS theory [5]. In the BCS theory, a phonon-mediated attraction leads to the binding of electrons at the

Fermi surface into composite bosons called Cooper pairs. Phonon-mediated superconductors are also called conventional superconductors.

There are different groups of unconventional superconductors not described by the BCS theory. In 1986 the first unconventional superconductor of the group of materials called cuprates, signified by CuO_2 layers that are hole-doped by other atoms in the compound [6], was discovered by Bednorz and Müller [7]. These materials can have a T_c of 30-160 K [7], pushing the boundaries of what critical temperatures could be achieved and exceeding the threshold of 77 K.

In 2001 Nagamatsu and coworkers were able to show superconductivity in MgB_2 at 39 K [8]. This is particularly interesting as a study by Bud'ko and coworkers in the same year that measured the effect of the B isotopes within the crystal, suggested that MgB_2 is a conventional superconductor [9]. The material being conventional allows its investigation within the BCS theory or its generalizations. However, the anisotropic electron-phonon interaction at the Fermi surface of MgB_2 makes the *ab initio* description of its superconducting properties very challenging. A first *ab initio* study within the Eliashberg theory by Choi and coworkers [10] was able to qualitatively describe the material and predict a good critical temperature T_c. Some of the methods used in Ref. [10], that lead to this T_c have been criticized [11, 12]. Another study by Margine and coworkers [13] came to a similar qualitative result however with a critical temperature significantly above the measured T_c. An investigation using superconducting density-functional theory by Floris and coworkers [14] was also not able to definitively address the discrepancy of T_c between theoretical studies and experimental values. Many other first-principles studies of MgB_2 [12, 15–19] do not investigate the superconducting phase or use the isotropic approximation to obtain a value for T_c. There are discrepancies among these existing studies of MgB_2 regarding phonon energies and electron-phonon interaction.

In this bachelor's thesis, we present an *ab initio* study of phonon-mediated superconductivity in MgB_2. In our study, we use an approach based on the Eliashberg theory [13], which is a generalization of the before-mentioned BCS theory. We treat the electron-phonon interaction as fully anisotropic in electron and phonon momentum. Within the Eliashberg theory, the Coulomb interaction is approximated by an isotropic pseudopotential parameter, μ^*. This parameter can be calculated from first principles but is often used as a free parameter. In our work, we use *ab initio* values for μ^* from Ref. [20]. The

necessary electron-phonon related quantities are calculated from first principles within the framework of density-functional (DFT) and density-functional perturbation (DFPT) theory [21, 22].

To perform these calculations, we use the full-potential all-electron code **exciting** [23] to numerically solve both the Kohn-Sham and Sternheimer equations, of DFT and DFPT, respectively. Then, we employ the *ab initio* transport code **elphbolt** [24] to solve the Eliashberg equations. Within our approach, we use Wannier interpolation, where quantities such as the electronic and phonon energies, as well as electron-phonon-coupling vertices, are interpolated using a real-space representation. The electron-phonon quantities in real-space representation are calculated by **exciting** and then transformed onto dense meshes in reciprocal space by **elphbolt**. We test the construction of real-space quantities in **exciting** and the new interface between the codes and validate the functionality of the implemented methods, applying our formalism to doped diamond under pressure. Last but not least, we employ these methods to study MgB_2. We calculate the relevant electron-phonon related quantities of MgB_2 from first principles and study the superconducting properties of the material within the Eliashberg theory. Additionally, we compare our results and other first-principles studies, to give some insight into the discrepancies between existing studies.

This thesis is organized into three main chapters. In Chapter 2 , we first introduce the theory of superconductivity that we employ within our study and then the framework based on DFT and DFPT used to calculate the necessary quantities from first principles. In Chapter 3, after presenting the general workflow of our calculations, we show our results for MgB_2 comparing them to other first-principles studies. Chapter 4 includes a final discussion of our results and the conclusions we are able to draw from our study.

Chapter 2

Theoretical Background

In this chapter, we show the theory we use for an *ab initio* description of superconductivity. We first introduce the phenomenon itself, followed by a discussion of the Bardeen-Cooper-Schrieffer (BCS) and the Eliashberg (ET) theory of superconductivity. Then, we discuss how the combined use of density-functional (DFT) and density-functional perturbation (DFPT) theory allows us to calculate the electronic and phonon energies, as well as the electron-phonon interaction vertices. These quantities are obtained for a finite set of eigenstates which can be expressed as Bloch wave functions and are calculated on a uniform grid of the first Brillouin Zone in reciprocal space. In the last sections, we introduce Wannier functions and Wannier interpolation which are used to obtain the relevant quantities on dense grids in reciprocal space.[1]

2.1 Superconductivity

In this section, we briefly discuss the phenomenon of superconductivity, as presented in Refs. [1, 25]. A superconductor is characterized by a critical temperature T_c, for temperatures T higher than T_c, the superconducting phase is broken and the material is in a normal phase. The electrodynamic behavior

[1]Notice that throughout this thesis we use atomic units, where the reduced Planck constant $\hbar$, electronic mass m_e, the electron charge e, as well as the dielectric ε_0 and Boltzmann k_B constants are set as $\hbar = m_\mathrm{e} = e = 4\pi\varepsilon_0 = k_\mathrm{B} = 1$.

of a superconductor can be described by the London equations [1],

$$\frac{\partial \mathbf{J}_\mathrm{s}}{\partial t} = \rho_\mathrm{s}\,\mathbf{E}\,, \tag{2.1}$$

$$\nabla \times \mathbf{J}_\mathrm{s} = -\rho_\mathrm{s}\,\mathbf{B}\,, \tag{2.2}$$

where $\mathbf{J}_\mathrm{s}$ is the superconducting current density, $\mathbf{B}$ the magnetic flux density, $\mathbf{E}$ the electric field, t the time, and ρ_s the density of superconducting electrons. Equation (2.1) describes perfect conductivity as there is no explicit resistance term. Furthermore, it can be shown, that combining Eq. (2.2) with the Maxwell equations one obtains the equations [25],

$$\nabla^2\mathbf{B} = 4\pi\,\rho_s\,\mathbf{B}\,, \tag{2.3}$$

$$\nabla^2\mathbf{J}_\mathrm{s} = 4\pi\,\rho_s\,\mathbf{J}_\mathrm{s}\,. \tag{2.4}$$

The solutions of these equations are exponentially decaying at the edge of the material, giving rise to the Meissner effect, where the magnetic field is expelled from the superconductor.

There are two types of superconductors, type I and type II. The superconducting phase in a type I superconductor is broken by magnetic fields above a critical magnetic field $\mathbf{H}_\mathrm{c}$ [1]. Type II superconductors have a lower critical field $\mathbf{H}_\mathrm{c}^{(1)}$ and an upper critical field $\mathbf{H}_\mathrm{c}^{(2)}$. For a magnetic field in between the two critical fields, the material is in a mixed state with superconducting and normal domains, giving rise to a weakened Meissner effect [1]. The superconducting state can also be broken in both types of superconductors by $\mathbf{J}_\mathrm{s}$ above a critical current density $\mathbf{J}_\mathrm{c}$.

The order parameter that characterizes the superconducting and the normal phases is called the gap $\Delta(T)$. It is zero in the normal phase and becomes nonzero in the superconducting phase. In the superconducting phase one can observe an energy gap of $2\Delta(T)$ in the electronic quasi-particle spectrum [1].

2.2 BCS theory

Here, we discuss the Bardeen-Cooper-Schrieffer (BCS) theory of superconductivity. A more comprehensive overview can be found in Ref. [25]. The BCS theory is based on the principle that two electrons at the Fermi surface can form a bound state if an attractive interaction is present. These Cooper-pair states have a total angular momentum of zero.

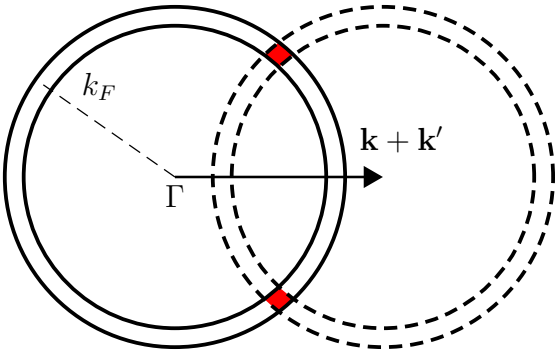

Figure 2.1: Sketch of a two-dimensional energy shell around a spherical Fermi surface with Fermi wave vector of length k_F. The red regions denote the available states for $\mathbf{k}$ and $\mathbf{k}'$. The two electrons can only exchange phonons of wave vector $\mathbf{q}$ such that $\mathbf{k}+\mathbf{q}$ is still within this region. This graphic is modeled similar to the one given in [26].

Within the BCS theory, the attractive interaction between two electrons is due to electron-phonon interaction. This source of pairing and the momentum and spin antisymmetry of the Cooper pairs are the signifying properties of conventional superconductors [6]. The energy of an electron scattering with a phonon can differ maximally by the highest phonon energy ω_D (Debye energy). This confines all electrons taking part in Cooper pairing to a small region around the Fermi surface. The phonon-mediated interaction between two electrons only affects the energy of the pair, if the wave function is antisymmetric with respect to spin [26].

The sketch in Fig. 2.1 shows the scattering phase space of pairing electrons with combined momentum $\mathbf{k}+\mathbf{k}'$ that exchange a single phonon. The initial and final states of the pairing electrons are confined to a small fraction of the shell around the Fermi surface (red areas in Fig. 2.1). This reduces the amount of phonons that can be exchanged between the pairing electrons and thus the phonon mediated interaction between the electrons. For $\mathbf{k}+\mathbf{k}'=\mathbf{0}$, the entire shell is available for scattering, maximizing the phonon-mediated interaction. Following these arguments, we can obtain the BCS Hamiltonian in the interaction picture, that only takes into account pair states of zero spin and momentum. In the rest of this section, we follow the approach given in Ref. [25]. The BCS Hamiltonian can be written as

$$\hat{H}_\mathrm{BCS} = \sum_{\mathbf{k}\,\sigma} \epsilon_\mathbf{k}\, c^\dagger_{\mathbf{k}\sigma}\, c_{\mathbf{k}\sigma} + \sum_{\mathbf{k}\,\mathbf{k}'} U(\mathbf{k},\mathbf{k}')\, c^\dagger_{\mathbf{k}\uparrow}\, c^\dagger_{-\mathbf{k}\downarrow}\, c_{-\mathbf{k}'\downarrow}\, c_{\mathbf{k}'\uparrow}\,, \tag{2.5}$$

where $c^{\dagger}_{\mathbf{k}\sigma}$ ($c_{\mathbf{k}\sigma}$) is the particle creation (annihilation) operator for a non-interacting electron of momentum $\mathbf{k}$ and spin σ and with energy $\epsilon_{\mathbf{k}}$ independent of spin. The Fermi energy ϵ_{F} is set to be zero. For the sake of simplicity, we omitted the band index n. The interaction potential, $U(\mathbf{k},\mathbf{k}')$, is approximated within the BCS theory by

$$U(\mathbf{k},\mathbf{k}') = \begin{cases} -U & \text{if } \epsilon_{\mathbf{k}}, \epsilon_{\mathbf{k}'} \in [-\omega_{\mathrm{D}}, \omega_{\mathrm{D}}]\,, \\ 0 & \text{otherwise,} \end{cases} \tag{2.6}$$

where U is a positive constant. Any Coulomb interaction with normal-state electrons is ignored within the BCS theory.

Applying a mean-field approximation to $\hat{H}_{\mathrm{BCS}}$ with respect to the thermal average of the pair operators $\langle c^{\dagger}_{\mathbf{k}\uparrow}\, c^{\dagger}_{-\mathbf{k}\downarrow}\rangle$, we get

$$\hat{H}^{(\mathrm{mf})}_{\mathrm{BCS}} = \sum_{\mathbf{k}\,\sigma} \epsilon_{\mathbf{k}}\, c^{\dagger}_{\mathbf{k}\sigma}\, c_{\mathbf{k}\sigma} - \sum_{\mathbf{k}} \Big[\Delta\, c^{\dagger}_{\mathbf{k}\uparrow}\, c^{\dagger}_{-\mathbf{k}\downarrow} + \Delta^{*}\, c_{-\mathbf{k}\uparrow}\, c_{\mathbf{k}\downarrow}\Big] + \text{const.}\,, \tag{2.7}$$

where we introduced the superconducting gap Δ defined as

$$\Delta = U \sum_{\mathbf{k}} \langle c_{-\mathbf{k}\downarrow}\, c_{\mathbf{k}\uparrow}\rangle\,. \tag{2.8}$$

The quantity Δ represents the order parameter for the transition to a superconducting state. Solutions for the BCS Hamiltonian can be found by applying the Nambu formalism, where we define a Matsubara Green's function matrix[2]

$$\underline{\underline{G}}(\mathbf{k},\tau) = \begin{pmatrix} G_{\mathrm{e}}(\mathbf{k},\tau) & F(\mathbf{k},\tau) \\ F^{*}(\mathbf{k},\tau) & G^{*}_{\mathrm{e}}(-\mathbf{k},\tau) \end{pmatrix} \tag{2.9}$$

with the standard electronic Green's function for the state momentum $\mathbf{k}$ given as

$$G_{\mathrm{e}}(\mathbf{k},\tau) = -\left\langle \hat{\mathcal{T}}\Big\{\, c_{\mathbf{k}\uparrow}(\tau)\, c^{\dagger}_{\mathbf{k}\uparrow}(0)\Big\}\right\rangle \tag{2.10}$$

on the main diagonal and Gor'kov's anomalous Green's function for the same electronic state

$$F(\mathbf{k},\tau) = -\left\langle \hat{\mathcal{T}}\Big\{\, c_{\mathbf{k}\uparrow}(\tau)\, c_{-\mathbf{k}\downarrow}(0)\Big\}\right\rangle \tag{2.11}$$

[2]The two underlying lines signify that $\underline{\underline{G}}(\mathbf{k},\tau)$ is a matrix.

on the off-diagonal terms. Here, $\hat{\mathcal{T}}$ is the time-ordering operator with respect to the imaginary time τ and the brackets $\langle\,\rangle$ denote a thermal average. We did not include the spin labels within the symbols of the Green's functions, as there is no spin-changing interaction within the theory.

As $\underline{\underline{G}}(\mathbf{k},\tau) = -\underline{\underline{G}}(\mathbf{k},\tau+\beta)$ with $\beta = 1/T$, we can expand this Green's function into a Fourier series

$$\underline{\underline{G}}(\mathbf{k},\tau) = \frac{1}{\beta}\sum_{j=-\infty}^{\infty} e^{-i\,\omega_j\tau}\,\underline{\underline{G}}(\mathbf{k},i\,\omega_j)\,, \tag{2.12}$$

the Fourier coefficients matrix $\underline{\underline{G}}(\mathbf{k},i\,\omega_j)$ represents the imaginary-frequency Matsubara Green's functions. Furthermore, in Eq. (2.12), we use the fermion Matsubara frequencies

$$\omega_j^{\mathrm{F}} \equiv \omega_j = \frac{2j+1}{\beta}\,\pi \qquad j\in\mathbb{Z}\,, \tag{2.13}$$

and we also define the bosonic Matsubara frequencies as

$$\omega_j^{\mathrm{B}} = \frac{2j}{\beta}\,\pi \qquad j\in\mathbb{Z}\,. \tag{2.14}$$

For the imaginary-frequency Matsubara Green's functions of the electronic quasi-particles, we get

$$G_{\mathrm{e}}(\mathbf{k},i\,\omega_j) = \frac{i\,\omega_j+\epsilon_{\mathbf{k}}}{(i\,\omega_j)^2-\epsilon_{\mathbf{k}}^2-|\Delta|^2}\,. \tag{2.15}$$

The corresponding retarded Green's function is found to have exactly the same form, replacing $i\,\omega_j$ with $\epsilon+i0^+$, where ϵ is a real energy and 0^+ is an infinitesimal positive number. We get the quasi-particle energies $\epsilon_{\mathrm{qp}}(\mathbf{k})$ from the poles of the Green's function at

$$\epsilon_{\mathrm{qp}}^2(\mathbf{k}) = \epsilon_{\mathbf{k}}^2 + |\Delta|^2\,, \tag{2.16}$$

giving rise to an energy gap of $2|\Delta|$ in the electronic quasi-particle spectrum.

2.3 Eliashberg theory

In this section, we summarize the Eliashberg theory (ET) of superconductivity as shown in Ref. [13]. ET is a strong-coupling generalization of the beforementioned BCS theory.

We write $\underline{\underline{G}}(n\mathbf{k}, i\,\omega_j)$ with band index n as electron-phonon interaction is band resolved in ET. We ignore cross-band pairing. Starting from the normal-state Matsubara Green's function $\underline{\underline{G}}^0(n\mathbf{k}, i\,\omega_j)$, the interacting Matsubara Green's function $\underline{\underline{G}}(n\mathbf{k}, i\,\omega_j)$ is obtained by solving the Dyson equation

$$\underline{\underline{G}}(n\mathbf{k}, i\,\omega_j) = \underline{\underline{G}}^0(n\mathbf{k}, i\,\omega_j) + \underline{\underline{G}}^0(n\mathbf{k}, i\,\omega_j) \cdot \underline{\underline{\Sigma}}(n\mathbf{k}, i\,\omega_j) \cdot \underline{\underline{G}}(n\mathbf{k}, i\,\omega_j)\,, \tag{2.17}$$

where the self-energy $\underline{\underline{\Sigma}}(n\mathbf{k}, i\,\omega_j)$ can include any interaction terms between time-reversed electronic states. Within ET, $\underline{\underline{\Sigma}}(n\mathbf{k}, i\,\omega_j)$ consists of an electron-phonon part and a Coulomb part. The Coulomb part only includes the interaction for the off-diagonal anomalous Green's functions.

In order to write the phonon part of the self energy, we define the non-interacting phonon Green's function

$$D(\nu\mathbf{q}, i\,\omega_j^{\mathrm{B}}) = \frac{2\,\omega_{\nu\mathbf{q}}}{(i\,\omega_j^{\mathrm{B}})^2 - \omega_{\nu\mathbf{q}}^2}, \tag{2.18}$$

where $\omega_{\nu\mathbf{q}}$ is the energy of the phonon mode of branch index ν and momentum $\mathbf{q}$.

Furthermore, using the identity $\underline{\underline{\sigma_0}}$ and the Pauli matrices

$$\underline{\underline{\sigma_1}} = \begin{pmatrix} 0 & 1 \\ 1 & 0 \end{pmatrix}, \qquad \underline{\underline{\sigma_2}} = \begin{pmatrix} 0 & -i \\ i & 0 \end{pmatrix}, \qquad \underline{\underline{\sigma_3}} = \begin{pmatrix} 1 & 0 \\ 0 & -1 \end{pmatrix} \tag{2.19}$$

to write the self energy, we obtain Eqs. (9-11) of Ref. [13],

$$\underline{\underline{\Sigma}}(n\mathbf{k}, i\,\omega_j) = \underline{\underline{\Sigma}}^{\mathrm{ep}}(n\mathbf{k}, i\,\omega_j) + \underline{\underline{\Sigma}}^{\mathrm{c}}(n\mathbf{k}, i\,\omega_j)\,, \tag{2.20}$$

where

$$\underline{\underline{\Sigma}}^{\mathrm{ep}}(n\mathbf{k}, i\,\omega_j) = -\frac{1}{\beta} \sum_{m\mathbf{k}',j',\nu} |g_{mn\nu}(\mathbf{k},\mathbf{q})|^2\, \underline{\underline{\sigma_3}} \cdot \underline{\underline{G}}(m\mathbf{k}', i\,\omega_j) \cdot \underline{\underline{\sigma_3}}\, D(\nu\mathbf{q}, i\,\omega_j - i\,\omega_{j'})\,, \tag{2.21}$$

$$\underline{\underline{\Sigma}}^{\mathrm{c}}(n\mathbf{k}, i\,\omega_j) = -\frac{1}{\beta} \sum_{m\mathbf{k}',j'} V_{\mathrm{ee}}(n\mathbf{k}, m\mathbf{k}')\, \underline{\underline{\sigma_3}} \cdot \begin{pmatrix} 0 & F(m\mathbf{k}', i\,\omega_j) \\ F^*(m\mathbf{k}', i\,\omega_j) & 0 \end{pmatrix} \cdot \underline{\underline{\sigma_3}}\,. \tag{2.22}$$

In Eqs. (2.21) and (2.22), $\underline{\underline{\Sigma}}^{\mathrm{ep}}(n\mathbf{k}, i\,\omega_j)$ is the electron-phonon and $\underline{\underline{\Sigma}}^{\mathrm{c}}(n\mathbf{k}, i\,\omega_j)$ the Coulomb part of the self-energy and the phonon momentum is $\mathbf{q} = \mathbf{k}' - \mathbf{k}$. $V_{\mathrm{ee}}(n\mathbf{k}, m\mathbf{k}')$ is the Coulomb interaction between the two electronic states and $g_{mn\nu}(\mathbf{k}, \mathbf{q})$ is the electron-phonon vertex.

At this point, we apply the standard approximations of ET given in Ref. [13]. The first approximation is already included in the self energy, as we only include the lowest-order term of the Feynman expansion. For the Coulomb interaction, we also include only its off-diagonal part, to prevent double counting of those parts already included in the Kohn-Sham Hamiltonian. Similar to the BCS theory, we consider electronic states within a certain region around the Fermi surface, and we approximate the normal-state electronic density of states to be constant $N(\epsilon) = N_{\mathrm{F}} \equiv N(\epsilon_{\mathrm{F}})$ within this region. The sums over Matsubara frequencies are also cut-off at a certain frequency and we replace the Coulomb interaction $N_{\mathrm{F}}\, V_{\mathrm{ee}}(n\mathbf{k}, m\mathbf{k}')$ with the Morel-Anderson pseudo potential μ^* [27].

The phonon-mediated interaction between electrons can be captured by introducing the Eliashberg spectral function

$$\begin{aligned} \alpha^2F(n\mathbf{k}, m\mathbf{k}', \omega) &= \sum_{\nu} \alpha^2F_{\nu}(n\mathbf{k}, m\mathbf{k}', \omega) \\ &= N_{\mathrm{F}} \sum_{\nu} |g_{mn\nu}(\mathbf{k}, \mathbf{q})|^2\, \delta(\omega - \omega_{\nu\mathbf{q}})\,, \end{aligned} \tag{2.23}$$

and the electron-phonon interaction function

$$\lambda(n\mathbf{k}, m\mathbf{k}', i\,\omega_j^{\mathrm{B}}) = \int_0^{\infty} d\omega\, \frac{2\omega}{(\omega_j^{\mathrm{B}})^2 + \omega^2}\, \alpha^2F(n\mathbf{k}, m\mathbf{k}', \omega)\,. \tag{2.24}$$

Isotropic and band-averaged versions of these quantities can be obtained by averaging over the Fermi surface

$$\alpha^2F(\omega) = \sum_{\nu} \alpha^2F_{\nu}(\omega) = \sum_{n\mathbf{k}, m\mathbf{k}', \nu} W_{n\mathbf{k}}\, W_{m\mathbf{k}'}\, \alpha^2F_{\nu}(n\mathbf{k}, m\mathbf{k}', \omega)\,, \tag{2.25}$$

$$\lambda(i\,\omega_j^{\mathrm{B}}) = \sum_{n\mathbf{k}, m\mathbf{k}'} W_{n\mathbf{k}}\, W_{m\mathbf{k}'}\, \lambda(n\mathbf{k}, m\mathbf{k}', i\,\omega_j^{\mathrm{B}}), \tag{2.26}$$

with $W_{n\mathbf{k}} = \delta(\epsilon_{\mathrm{F}} - \epsilon_{\mathrm{N}}(n\mathbf{k}))/N_{\mathrm{F}}$, where $\epsilon_{\mathrm{N}}(n\mathbf{k})$ is the normal-state electronic energy. We also define the electron-phonon-coupling strength $\lambda = \lambda(0)$ as

a measure for the electron-phonon interaction within the system. Using the anisotropic quantities, we can write the Eliashberg equations for the mass renormalization $Z(n\mathbf{k}, i\,\omega_j)$ and the gap function $\Delta(n\mathbf{k}, i\,\omega_j)$ as [13],

$$Z(n\mathbf{k}, i\,\omega_j) = 1 + \frac{\pi\,T}{\omega_j} \sum_{m\mathbf{k}',j'} W_{m\mathbf{k}'}\,\lambda(n\mathbf{k}, m\mathbf{k}', i\,\omega_j - i\,\omega_{j'})\,\frac{\omega_{j'}}{\sqrt{\omega_{j'}^2 + \Delta^2(n\mathbf{k}', i\,\omega_{j'})}} \tag{2.27}$$

and

$$\Delta(n\mathbf{k}, i\,\omega_j)\,Z(n\mathbf{k}, i\,\omega_j) = \pi\,T \sum_{m\mathbf{k},'j'} W_{m\mathbf{k}'}\,[\lambda(n\mathbf{k}, m\mathbf{k}', i\,\omega_j - i\,\omega_{j'}) - \mu^*]\,\frac{\Delta(m\mathbf{k}', i\,\omega_{j'})}{\sqrt{\omega_{j'}^2 + \Delta^2(m\mathbf{k}', i\,\omega_{j'})}}. \tag{2.28}$$

Equations (2.27) and (2.28) have to be solved self consistently. Similar to Eq. (2.16), the quasi-particle energies are given by the poles of the retarded Green's function as

$$\epsilon_{\rm qp}^2(n\mathbf{k}) = \frac{\epsilon_{\rm N}^2(n\mathbf{k})}{Z^2(n\mathbf{k}, \epsilon(n\mathbf{k}))} + \Delta^2\Big(n\mathbf{k}, \epsilon(n\mathbf{k})\Big). \tag{2.29}$$

At the Fermi surface $\epsilon_{\rm N}(n\mathbf{k}) = 0$. We can thus find the gap function at the Fermi surface, called the leading edge

$$\Delta_{n\mathbf{k}}^{(\rm F)} = \Re\Big[\,\Delta(n\mathbf{k}, \Delta_{n\mathbf{k}}^{(\rm F)})\,\Big] \tag{2.30}$$

and the electronic quasi-particle density of states obtained from the imaginary part of the retarded greens function [10]

$$N(\omega) = N_{\rm F} \sum_{n\mathbf{k}} W_{n\mathbf{k}} \Re\left[\frac{\omega + i0^+}{\sqrt{(\omega + i0^+)^2 - \Delta^2(n\mathbf{k}, \omega)}}\right]. \tag{2.31}$$

We evaluate $\Delta(\mathbf{k}, \omega)$ using an N-point Padé approximation given in Eqs. (A2) and (A3) of Ref. [28].

2.4 Density-functional theory

To calculate $\lambda(n\mathbf{k}, m\mathbf{k}', i\,\omega_j^{\mathrm{B}})$ and to solve Eqs. (2.27) and (2.28), we have to compute the energies of electrons $\epsilon_{n\mathbf{k}}$ and phonons $\omega_{\nu\mathbf{q}}$, as well as the electron-phonon interaction vertices $g_{mn\nu}(\mathbf{k}, \mathbf{q})$. To this purpose, we use the framework of density-functional theory (DFT).

We start this section by summarizing as DFT can be derived from the full many-body Schrödinger equation for the combined system of electrons and nuclei

$$\hat{H}(\mathfrak{r}, \mathcal{R})\, \Psi(\mathfrak{r}, \mathcal{R}) = E\, \Psi(\mathfrak{r}, \mathcal{R}). \tag{2.32}$$

In Eq. (2.32), we write $\mathfrak{r} = \{\mathbf{r}_i\}$ for the set of electron positions and $\mathcal{R} = \{\mathbf{R}_I\}$ for the set of nuclear positions. The Hamiltonian $\hat{H}(\mathfrak{r}, \mathcal{R})$ that describes the combined system can be separated into an electronic and a nuclear part

$$\hat{H}(\mathfrak{r}, \mathcal{R}) = \hat{H}_{\mathrm{e}}(\mathfrak{r}, \mathcal{R}) + \hat{H}_{\mathrm{n}}(\mathcal{R})\,, \tag{2.33}$$

where

$$\hat{H}_{\mathrm{e}}(\mathfrak{r}, \mathcal{R}) = \hat{T}_{\mathrm{e}} + V_{\mathrm{ee}}(\mathfrak{r}) + V_{\mathrm{en}}(\mathfrak{r}, \mathcal{R})\,, \tag{2.34}$$

$$H_{\mathrm{n}}(\mathcal{R}) = \hat{T}_{\mathrm{n}} + V_{\mathrm{nn}}(\mathcal{R})\,. \tag{2.35}$$

In these equations, the kinetic-energy operator $\hat{T}_a$ is the sum of all single-particle kinetic-energy operators for all particles of type a. $V_{ab}(\mathfrak{r})$ is the full Coulomb interaction among particles of type a and particles of type b, excluding self-interaction terms for $a = b$. The particles a, b are either electrons (e) or nuclei (n).

Within the Born-Oppenheimer approximation, the total wave function can be factorized as a product of an electronic and a nuclear wave function

$$\Psi(\mathfrak{r}, \mathcal{R}) = \Phi(\mathfrak{r}, \mathcal{R})\, \chi(\mathcal{R}) \tag{2.36}$$

where the factors satisfy the following Schrödinger-like equations

$$\hat{H}_{\mathrm{e}}(\mathfrak{r}, \mathcal{R})\, \Phi(\mathfrak{r}, \mathcal{R}) = E_{\mathrm{e}}^{\mathcal{R}}\, \Phi(\mathfrak{r}, \mathcal{R})\,, \tag{2.37}$$

$$\left[H_{\mathrm{n}}(\mathcal{R}) + E_{\mathrm{e}}^{\mathcal{R}}\right] \chi(\mathcal{R}) = E\chi(\mathcal{R})\,. \tag{2.38}$$

Under these conditions, we can obtain

$$\Phi_0(\mathfrak{r}, \mathcal{R}) \approx \Phi_0(\mathfrak{r}, \langle \mathcal{R} \rangle) \equiv \Phi_0^{\langle \mathcal{R} \rangle}(\mathfrak{r}) \tag{2.39}$$

for the ground state of the electronic Hamiltonian $\hat{H}_\mathrm{e}$. Here, $\Phi_0^{\mathcal{R}}$ is the ground state of the electronic system for the nuclear configuration $\mathcal{R}$ and $\langle \mathcal{R} \rangle$ is the equilibrium configuration of the nuclei. This approximation is valid because of the mass difference between nuclei and electrons.

Assuming to have a system with fixed nuclear positions at $\langle \mathcal{R} \rangle$, we only have to solve the Schrödinger equation for the electronic Hamiltonian

$$\hat{H}_\mathrm{e}(\mathfrak{r}, \langle \mathcal{R} \rangle) = \sum_i \frac{\hat{\mathbf{p}}_i^2}{2} + V_\mathrm{ee}(\mathfrak{r}, \langle \mathcal{R} \rangle) + V_\mathrm{ext}(\mathfrak{r}, \langle \mathcal{R} \rangle)\,. \tag{2.40}$$

The explicit dependence on $\langle \mathcal{R} \rangle$ is omitted in the next part of this chapter. The external potential in Eq. (2.40) is defined as

$$V_\mathrm{ext}(\mathfrak{r}) = V_\mathrm{en}(\mathfrak{r}) = \sum_i v_\mathrm{ext}(\mathbf{r}_i) \tag{2.41}$$

in terms of the single-electron potential $v_\mathrm{ext}(\mathbf{r})$.

According to the Hohenberg-Kohn theorem [21], there is a bijection between the external potential $v_\mathrm{ext}(\mathbf{r})$ and the electronic ground-state density $\rho_0(\mathbf{r})$

$$v_\mathrm{ext}(\mathbf{r}) \Rightarrow \hat{H}(\mathfrak{r}) \Rightarrow \Phi(\mathfrak{r}) \Rightarrow \rho_0(\mathbf{r}) \Rightarrow v_\mathrm{ext}(\mathbf{r}). \tag{2.42}$$

This tells us that all quantities related to the electronic system can be found as a functional of the ground-state electron density $\rho_0(\mathbf{r})$. In order to calculate this density and the ground-state energy E_0, we introduce the non-interacting Kohn-Sham (KS) system [29], which is described by the following (KS) equations

$$\hat{h}^\mathrm{KS}(\mathbf{r})\, \varphi_i^\mathrm{KS}(\mathbf{r}) = \epsilon_i\, \varphi_i^\mathrm{KS}(\mathbf{r})\,, \tag{2.43}$$

where

$$\hat{h}^\mathrm{KS}(\mathbf{r}) = \frac{1}{2}\hat{\mathbf{p}}^2 + v^\mathrm{KS}(\mathbf{r})\,, \tag{2.44}$$

$$v^\mathrm{KS}(\mathbf{r}) = \int d^3\mathbf{r}'\, \frac{\rho_0(\mathbf{r}')}{|\mathbf{r} - \mathbf{r}'|} + v_\mathrm{xc}[\rho_0](\mathbf{r}) + v_\mathrm{ext}(\mathbf{r})\,, \tag{2.45}$$

$$\rho_0(\mathbf{r}) = \sum_i^\mathrm{occ} |\varphi_i^\mathrm{KS}(\mathbf{r})|^2\,. \tag{2.46}$$

Equations (2.43-2.46) have to be solved self consistently. In order to keep an easy notation, we drop the label KS going forward. The KS single-electron Hamiltonian $\hat{h}(\mathbf{r})$ and wave function $\varphi_i(\mathbf{r})$ describe the auxiliary system of non-interacting electrons. $v_{\mathrm{xc}}[\rho](\mathbf{r})$ is the exchange and correlation potential that is unknown and has to be approximated. The energy of the electronic many-body system is given by

$$E_{\mathrm{e}} \equiv E_0[\rho] \equiv E[\rho] = \sum_i^{\mathrm{occ}} \epsilon_i + E_{\mathrm{I}}[\rho] - \int d^3\mathbf{r}\, \frac{\delta E_{\mathrm{I}}[\rho]}{\delta \rho(\mathbf{r})}\, \rho(\mathbf{r}) \tag{2.47}$$

where

$$E_{\mathrm{I}}[\rho] = \int d^3\mathbf{r}\, d^3\mathbf{r}'\, \frac{\rho(\mathbf{r})\rho(\mathbf{r}')}{|\mathbf{r}-\mathbf{r}'|} + E_{\mathrm{xc}}[\rho]. \tag{2.48}$$

For a direct application of the DFT to the materials studied in this thesis, we have to give a clear definition of the reference, equilibrium nuclear configuration $\langle \mathcal{R} \rangle$. For a periodic crystal, the index I can be separated into a Bravais vector $\mathbf{R}$, which identifies the unit cell, and the index κ, which labels the nucleus at position $\mathbf{x}_\kappa$ in the unit cell. Therefore, we can write

$$I \equiv (\mathbf{R}, \kappa)\,. \tag{2.49}$$

According to this, the nuclear positions in the equilibrium configuration can be written as

$$\mathbf{R}_I = \mathbf{R} + \mathbf{x}_\kappa\,. \tag{2.50}$$

A generic displacement of the atom labeled with I can be denoted by $\mathbf{u}_\kappa^{\mathbf{R}}$.

2.5 Density-functional perturbation theory

In this section, we show how to calculate the dynamical matrix and its eigenvalues, starting from the ground-state energy acquired from density-functional theory. The theory presented here follows the work in [22] and [30]. Using a fixed equilibrium reference configuration $\langle \mathcal{R} \rangle \equiv \{\mathbf{R} + \mathbf{x}_\kappa\}$, we can expand the electronic energy into a Taylor series with respect to the atomic displacements $u_{\kappa\alpha}^{\mathbf{R}}$, where α labels the Cartesian components, as[3]

$$E(\{\mathbf{u}_\kappa^{\mathbf{R}}\}) = E_0 + \sum_{\kappa\alpha\mathbf{R}} \underbrace{\left.\frac{\partial E}{\partial u_{\kappa\alpha}^{\mathbf{R}}}\right|_0}_{=0} u_{\kappa\alpha}^{\mathbf{R}} + \frac{1}{2}\sum_{\kappa\alpha\mathbf{R}}\sum_{\kappa'\alpha'\mathbf{R}'} \left.\frac{\partial^2 E}{\partial u_{\kappa\alpha}^{\mathbf{R}} \partial u_{\kappa'\alpha'}^{\mathbf{R}'}}\right|_0 u_{\kappa\alpha}^{\mathbf{R}}\, u_{\kappa'\alpha'}^{\mathbf{R}'} + \mathcal{O}(u^3)\,. \tag{2.51}$$

[3]The symbol $|_0$ denotes the derivative being calculated at equilibrium (*i.e.*, at $\langle \mathcal{R} \rangle$).

In this equation, E_0 is simply the ground-state energy calculated from DFT at $\langle \mathcal{R} \rangle$, while the first-order term vanishes due to the equilibrium conditions. The second-order derivatives of the energy are called inter-atomic force constants

$$\Phi^{\mathbf{R},\mathbf{R}'}_{\kappa\alpha,\kappa'\alpha'} \equiv \left. \frac{\partial^2 E}{\partial u^{\mathbf{R}}_{\kappa\alpha}\, \partial u^{\mathbf{R}'}_{\kappa'\alpha'}} \right|_0 . \tag{2.52}$$

After this consideration, the dynamical matrix is defined as the mass-renormalized Fourier transform of the inter-atomic force constants

$$D_{\kappa\alpha,\kappa'\alpha'}(\mathbf{q}) = \frac{1}{\sqrt{m_\kappa\, m_{\kappa'}}} \sum_{\mathbf{R}} \Phi^{\mathbf{0},\mathbf{R}}_{\kappa\alpha,\kappa'\alpha'}\, \mathrm{e}^{i\mathbf{q}\cdot\mathbf{R}}, \tag{2.53}$$

where m_κ denotes the atomic mass and the summation is reduced to only one lattice vector, due to the translational invariance of the crystal. We can diagonalize the dynamical matrix using a unitary transformation with elements $e_{\kappa\alpha\nu}(\mathbf{q})$ such that

$$D_{\nu,\nu'}(\mathbf{q}) \equiv \sum_{\kappa\alpha,\kappa'\alpha'} e^{\dagger}_{\nu\kappa\alpha}(\mathbf{q})\, D_{\kappa\alpha,\kappa'\alpha'}(\mathbf{q})\, e_{\kappa'\alpha'\nu'}(\mathbf{q}) = \omega^2_{\nu\mathbf{q}} \delta_{\nu\nu'} \,, \tag{2.54}$$

where we introduce the phonon branch index ν and we write $e^{\dagger}_{\nu\kappa\alpha}(\mathbf{q})$ for the matrix elements of the inverse of $e_{\kappa\alpha\nu}(\mathbf{q})$ given by

$$e^{\dagger}_{\nu\kappa\alpha}(\mathbf{q}) \equiv e^{*}_{\kappa\alpha\nu}(\mathbf{q}) \,, \tag{2.55}$$

such that the indices of the dynamical matrix are always the first and the last index appearing in the sum. According to this definition, the elements $e_{\kappa\alpha\nu}(\mathbf{q})$ can be identified as the components of the normalized phonon eigenvectors of the dynamical matrix. The nuclear displacements, corresponding to an eigenstate of the dynamical matrix with branch index ν and momentum $\mathbf{q}$ are [31]

$$u^{\mathbf{R}}_{\kappa\alpha\nu}(\mathbf{q}) = \frac{1}{\sqrt{m_\kappa}}\, e_{\kappa\alpha\nu}(\mathbf{q})\, \mathrm{e}^{i\mathbf{q}\cdot\mathbf{R}} \equiv u_{\kappa\alpha\nu}(\mathbf{q})\, \mathrm{e}^{i\mathbf{q}\cdot\mathbf{R}} \,. \tag{2.56}$$

So far in this section, we have introduced the dynamical matrix and its eigenvectors. To calculate these for a given $\mathbf{q}$, we choose a number of orthogonal collective displacements $\{u_{\kappa\alpha\gamma}(\mathbf{q})\}$, that can be written as in Eq. (2.56) equal to the number of phonon branches. We write $u_{\kappa\alpha\gamma}(\mathbf{q})$ with the index γ replacing the band index ν for the displacement fields of these collective dis-

placements and to simplify notation, we also define the differential operator

$$\partial_{\gamma\mathbf{q}} \equiv \sum_{\kappa\alpha\mathbf{R}} u_{\kappa\alpha\gamma}(\mathbf{q})\, \mathrm{e}^{i\mathbf{q}\cdot\mathbf{R}}\, \left.\frac{\partial}{\partial u^{\mathbf{R}}_{\kappa\alpha}}\right|_0 . \tag{2.57}$$

Using this notation, we can write the dynamical matrix as [22],

$$\begin{aligned} D_{\gamma\gamma'}(\mathbf{q}) &= \partial_{\gamma\mathbf{q}}\partial_{\gamma'\mathbf{q}} E_{\mathrm{e}} \\ &= \sum_{i}^{\mathrm{occ}} \Big[\langle \partial_{\gamma\mathbf{q}}\varphi_i | \partial_{\gamma'\mathbf{q}} v_{\mathrm{ext}} | \varphi_i \rangle + \langle \varphi_i | \partial_{\gamma\mathbf{q}} v_{\mathrm{ext}} | \partial_{\gamma'\mathbf{q}}\varphi_i \rangle \\ &\quad + \langle \varphi_i | \partial_{\gamma\mathbf{q}}\partial_{\gamma'\mathbf{q}} v_{\mathrm{ext}} | \varphi_i \rangle + \langle \partial_{\gamma\mathbf{q}}\varphi_i | \hat{h} - \epsilon_i | \partial_{\gamma'\mathbf{q}}\varphi_i \rangle \Big] \\ &\quad + \frac{1}{2} \int d^3\mathbf{r}\, d^3\mathbf{r}'\, \frac{\delta^2 E_{\mathrm{I}}[\rho]}{\delta\rho(\mathbf{r})\, \delta\rho(\mathbf{r}')}\, \partial_{\gamma\mathbf{q}}\rho(\mathbf{r})\, \partial_{\gamma'\mathbf{q}}\rho(\mathbf{r}') , \end{aligned} \tag{2.58}$$

where eigenstates of the dynamical matrix can be obtained by diagonalizing it. To compute $\partial_{\gamma\mathbf{q}}\varphi_i(\mathbf{r})$ and $\partial_{\gamma\mathbf{q}}\rho(\mathbf{r})$, we have to expand the quantities in Eq. (2.43) into a power series in $\partial_{\gamma\mathbf{q}}$. Proceeding in this way, the first-order terms in Eq. (2.43) can be collected to recover the Sternheimer equation

$$\Big[\partial_{\gamma\mathbf{q}} h(\mathbf{r}) - \partial_{\gamma\mathbf{q}}\epsilon_i\Big]\, \varphi_i(\mathbf{r}) = -\Big[\hat{h}(\mathbf{r}) - \epsilon_i\Big]\, \partial_{\gamma\mathbf{q}}\varphi_i(\mathbf{r}) . \tag{2.59}$$

This equation has to be solved self consistently, as $\partial_{\gamma\mathbf{q}} h(\mathbf{r})$ and $\partial_{\gamma\mathbf{q}}\varphi_i(\mathbf{r})$ are coupled by the taylor expansions of Eqs. (2.44-2.46).

2.6 Wannier functions

In this section, we discuss the theory of Wannier functions (WFs) which is also presented in Ref. [32]. WFs form an orthogonal basis of localized wave functions, similar to atomic-like functions.

The eigenstates of the Kohn-Sham Hamiltonian can be written in terms of Bloch wave functions with reciprocal lattice vector $\mathbf{k}$ and band index n defined as[4]

$$\varphi_{n\mathbf{k}}(\mathbf{r}) = a_{n\mathbf{k}}(\mathbf{r})\, \mathrm{e}^{i\mathbf{k}\cdot\mathbf{r}} , \tag{2.60}$$

where $a_{n\mathbf{k}}(\mathbf{r})$ is periodic with respect to any $\mathbf{R}$. These Bloch wave functions are calculated for a set of reciprocal lattice vectors $\mathbf{k}$, that form a uniform grid

[4]Rewriting the index i of the eigenstates of the Kohn-Sham Hamiltonian as $i \equiv (n, \mathbf{k})$.

of the Brilloin Zone. The total number of grid points is denoted as N_e.

From this, we construct a set of maximally localized WFs, that can be used to interpolate electronic quantities from a coarse to a dense **k**-grid. This is necessary because dense electronic **k** and phonon **q** meshes are necessary to properly describe electron-phonon interaction within solids.

A set of orthogonal Wannier functions $w_n^{\mathbf{R}}(\mathbf{r})$, corresponding to a set of orthogonal Bloch wave functions $\phi_{n\mathbf{k}}(\mathbf{r})$ on a uniform grid in reciprocal space **k** with band index n, can be constructed via a Fourier transformation [33]

$$w_n^{\mathbf{R}}(\mathbf{r}) = \frac{1}{N_\mathrm{e}} \sum_{\mathbf{k}} \mathrm{e}^{-i\mathbf{k}\cdot\mathbf{R}}\, \phi_{n\mathbf{k}}(\mathbf{r}) \tag{2.61}$$

with

$$w_n^{\mathbf{R}}(\mathbf{r}) = w_n^{\mathbf{0}}(\mathbf{r} - \mathbf{R})\,. \tag{2.62}$$

We can find a different orthogonal Wannier basis for the same space if we apply a unitary transformation with elements $U_{mn}(\mathbf{k})$,

$$\tilde{w}_n^{\mathbf{R}}(\mathbf{r}) = \frac{1}{N_\mathrm{e}} \sum_{m\mathbf{k}} e^{-i\mathbf{k}\cdot\mathbf{R}}\, U_{mn}(\mathbf{k})\, \phi_{m\mathbf{k}}(\mathbf{r}), \tag{2.63}$$

giving us control over the shape of the WFs. We use this freedom of choice by constructing a set of maximally localized WFs with respect to the minimization of the spread [33],

$$\Xi = \sum_n \langle w_n^{\mathbf{0}}|\, \mathbf{r}^2\, |w_n^{\mathbf{0}}\rangle - \langle w_n^{\mathbf{0}}|\, \mathbf{r}\, |w_n^{\mathbf{0}}\rangle^2\,. \tag{2.64}$$

To construct WFs that form a basis for a given energy window with lower (upper) bound ϵ_low (ϵ_up) we define a subspace $A(J)$ of the single-particle Hilbert space of Kohn-Sham wave functions $\varphi_{n\mathbf{k}}(\mathbf{r})$ such that

$$\epsilon_{n\mathbf{k}} \in [\epsilon_\mathrm{low}, \epsilon_\mathrm{up}] \Rightarrow \varphi_{n\mathbf{k}}(\mathbf{r}) \in A(J)\,, \tag{2.65}$$

where J is the number of states at each **k** point within the subspace. A subspace $A(J)$ can be built using a semi-unitary transformation with elements $\mathcal{U}_{lm}(\mathbf{k})$ from a $\mathcal{J}_\mathbf{k} \geq J$ to the J dimensional subspace, that mixes bands outside the energy window and leaves states within the window unchanged.

This process is called disentanglement [33]. Once the bands are disentangled, we can construct maximally localized WFs within $A(J)$ by utilizing a unitary transformation as in Eq. (2.63), resulting in WFs of the form

$$w_n^{\mathbf{R}}(\mathbf{r}) = \frac{1}{N_\mathrm{e}} \sum_{m,l\mathbf{k}} e^{-i\mathbf{k}\cdot\mathbf{R}}\, U_{mn}(\mathbf{k})\, \mathcal{U}_{lm}(\mathbf{k})\, \varphi_{l\mathbf{k}}(\mathbf{r})\,. \tag{2.66}$$

For the best localization, both $\mathcal{U}_{lm}(\mathbf{k})$ and $U_{mn}(\mathbf{k})$ have to be optimized at the same time. In order to recover the band structure of $A(J)$, we can apply the reverse transformation given by

$$\varphi_{n\mathbf{k}}(\mathbf{r}) = \sum_{m\mathbf{R}} \mathrm{e}^{i\mathbf{k}\cdot\mathbf{R}}\, U^\dagger_{mn}(\mathbf{k})\, w_m^{\mathbf{0}}(\mathbf{r}-\mathbf{R}). \tag{2.67}$$

This transformation can be done for an arbitrary $\mathbf{k}$ in reciprocal space and the matrix elements $U^\dagger_{nm}(\mathbf{k})$ at that $\mathbf{k}$ have to be chosen such that the Hamiltonian

$$h_{nm}(\mathbf{k}) \equiv \langle n\mathbf{k}|\, \hat{h}\, |m\mathbf{k}\rangle = \epsilon_{n\mathbf{k}}\, \delta_{nm} \tag{2.68}$$

is diagonal at this $\mathbf{k}$.

Using this method, we are able to interpolate quantities calculated on a coarse grid using DFT/DFPT to denser $\mathbf{k}$ meshes. This interpolation can be invalid outside and at the edges of the energy window, $[\epsilon_\mathrm{low}, \epsilon_\mathrm{up}]$ as $A(J)$ does not necessarily contain eigenstates of the Hamiltonian within that region.

2.7 Electron-phonon interaction

Within Eliashberg theory, electron-phonon interaction is the mechanism behind Cooper pairing. In this section we discuss, how the electron-phonon interaction matrix is calculated using DFPT and then how we interpolate it, the KS-Hamiltonian $h_{mn}(\mathbf{k})$ and the dynamical matrix $D_{\nu\nu'}(\mathbf{q})$ to finer meshes using WFs.

The electron-phonon interaction vertices are calculated as [31]

$$g_{mn\nu}(\mathbf{k},\mathbf{q}) = \langle m\mathbf{k}+\mathbf{q}|\, \partial_{\nu\mathbf{q}} v\, |n\mathbf{k}\rangle\,, \tag{2.69}$$

where v is the Kohn-Sham potential in Eq. (2.45). Similar to the electronic WFs, we can make a phonon Wannier transformation using $e_{\kappa\alpha\nu}(\mathbf{q})$ instead of $U^\dagger_{mn}(\mathbf{k})$.

We can use both phonon and electronic (Eq. (2.63)) Wannier transformations to transform the Hamiltonian [31]

$$h_{mn}(\mathbf{R}_\mathrm{e}, \mathbf{0}) = \frac{1}{N_\mathrm{e}} \sum_{n',m'\mathbf{k}} \mathrm{e}^{-i\mathbf{k}\cdot\mathbf{R}_\mathrm{e}}\, U^\dagger_{mm'}(\mathbf{k})\, h_{m'n'}(\mathbf{k})\, U_{n'n}(\mathbf{k})\,, \tag{2.70}$$

the dynamical matrix

$$D_{\kappa\alpha,\kappa'\alpha'}(\mathbf{R}_\mathrm{p}, \mathbf{0}) = \frac{1}{N_\mathrm{p}} \sum_{\nu,\nu'\mathbf{q}} \mathrm{e}^{-i\mathbf{q}\cdot\mathbf{R}_\mathrm{p}}\, e_{\kappa\alpha\nu}(\mathbf{q})\, D_{\nu\nu'}(\mathbf{q})\, e^\dagger_{\nu'\kappa'\alpha'}(\mathbf{q})\,, \tag{2.71}$$

and the electron-phonon interaction matrix

$$\begin{aligned} g_{mn\kappa\alpha}(\mathbf{R}_\mathrm{e}, \mathbf{R}_\mathrm{p}) = &\frac{1}{N_\mathrm{e}\, N_\mathrm{p}} \sum_{n',m'\mathbf{k}} \sum_{\nu\mathbf{q}} \mathrm{e}^{-i(\mathbf{k}\cdot\mathbf{R}_\mathrm{e}+\mathbf{q}\cdot\mathbf{R}_\mathrm{p})}\, u^{-1}_{\nu\kappa\alpha}(\mathbf{q}) \\ &\times U^\dagger_{mm'}(\mathbf{k}+\mathbf{q})\, g_{m'n'\nu}(\mathbf{k},\mathbf{q})\, U_{n'n}(\mathbf{k}) \end{aligned} \tag{2.72}$$

into the Wannier basis with electronic (phonon) lattice vector $\mathbf{R}_\mathrm{e}$ ($\mathbf{R}_\mathrm{p}$). Analogous to the back transformation of the Wannier basis Eq. (2.67), we can apply the back transformations to these matrices in order to interpolate them onto arbitrary $\mathbf{k}$ and $\mathbf{q}$ vectors in reciprocal space

$$h_{mn}(\mathbf{k}, \mathbf{0}) = \sum_{n',m'\mathbf{R}_\mathrm{e}} \mathrm{e}^{i\mathbf{k}\cdot\mathbf{R}_\mathrm{e}}\, U_{mm'}(\mathbf{k})\, h_{m'n'}(\mathbf{R}_\mathrm{e}, 0)\, U^\dagger_{n'n}(\mathbf{k})\,, \tag{2.73}$$

$$D_{\nu\nu'}(\mathbf{q}) = \sum_{\kappa\alpha,\kappa'\alpha'\mathbf{R}_\mathrm{p}} \mathrm{e}^{i\mathbf{k}\cdot\mathbf{R}_\mathrm{p}}\, e^\dagger_{\nu\kappa\alpha}(\mathbf{q})\, D_{\kappa\alpha\kappa'\alpha'}(\mathbf{R}_\mathrm{p}, \mathbf{0})\, e_{\kappa'\alpha'\nu'}(\mathbf{q})\,, \tag{2.74}$$

$$\begin{aligned} g_{mn\nu}(\mathbf{k}, \mathbf{q}) = &\sum_{n',m'\mathbf{R}_\mathrm{e}} \sum_{\nu\mathbf{R}_p} \mathrm{e}^{i(\mathbf{k}\cdot\mathbf{R}_\mathrm{e}+\mathbf{q}\mathbf{R}_p)} u_{\kappa\alpha\nu}(\mathbf{q}) \\ &\times U_{mm'}(\mathbf{k}+\mathbf{q})\, g_{m'n'\kappa\alpha}(\mathbf{R}_\mathrm{e}, \mathbf{R}_p)\, U^\dagger_{n'n}(\mathbf{k})\,. \end{aligned} \tag{2.75}$$

The components of the eigenvectors $e_{\nu\kappa\alpha}(\mathbf{q})$ can be obtained at any $\mathbf{q}$ analogous to $U_{mn}(\mathbf{k})$, as the dynamical matrix $D_{\nu\nu'}(\mathbf{q})$ has to be diagonal.

Chapter 3

Methods and Results

In the previous chapter, we established the theoretical framework of our calculations. Here, we discuss our methodology and results. First, we give some general information about our workflow, then, we present a test calculating λ for a simple material, testing the new features of the software packages **exciting** and **elphbolt** that we use in this work.

We perform this validation of our workflow by calculating the Eliashberg spectral function $\alpha^2F(\omega)$ and λ of doped pressurized diamond and compare our results to a similar calculation from Giustino and coworkers [31]. Then, we present our results for MgB_2 starting with the electronic and phonon band structures. Furthermore, we discuss the electron-phonon-coupling strength and the relevant phonon energies in comparison with different first-principles studies already present in the literature [10, 12, 13, 15–19, 34]. Finally, we present our results for the superconducting state, *e.g.*, the leading edge of the superconducting gap $\Delta^{(\mathrm{F})}_{n\mathbf{k}}$ and the critical temperature T_c.

3.1 Workflow

A diagrammatic representation of our workflow combining density-functional (DFT), density-functional perturbation (DFPT), and Eliashberg (ET) theory is shown in Fig. 3.1.

We first perform a relaxation of the crystal to obtain the equilibrium configuration $\langle \mathcal{R} \rangle$. For this, we fit the energy of the electronic system E_e to a set of primitive unit-cell volumes Ω and converge this fit. For the hexagonal crystal, we minimize E_e at each Ω with respect to the ratio of lattice con-

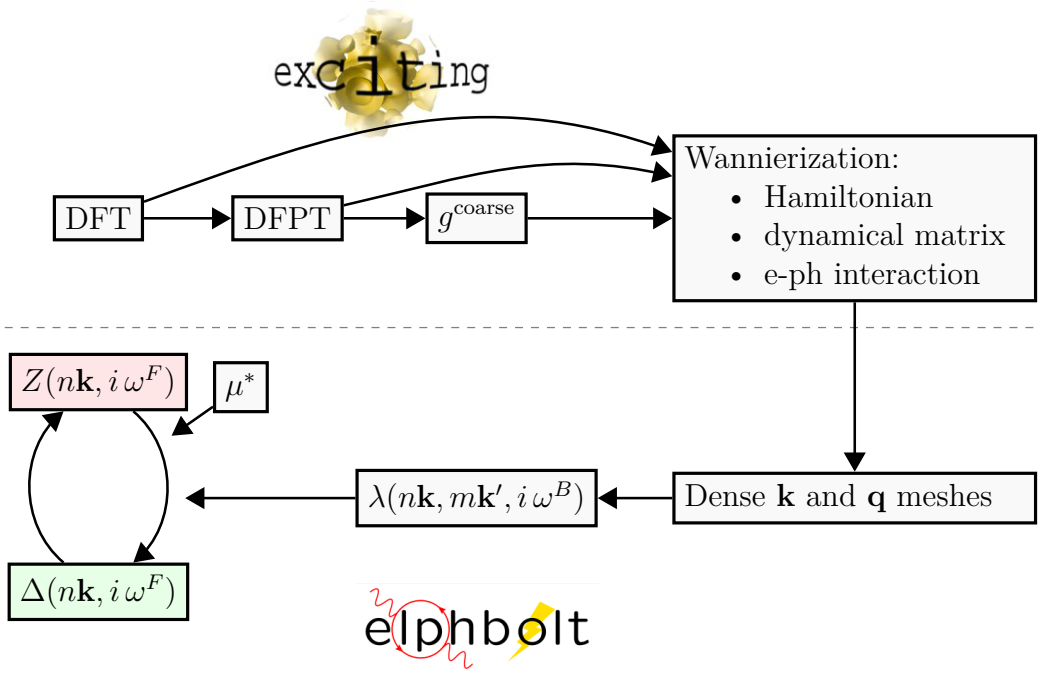

Figure 3.1: Workflow diagram for combining Eliashberg theory with DFT-based methods.

stants, fitting both E_{e} and the ratio of lattice constants as a function of Ω, we obtain $\langle \mathcal{R} \rangle$ as the minimum of E_{e}. We then perform an additional convergence test of both electronic ($\mathbf{k}$) and phonon ($\mathbf{q}$) grids in reciprocal space and calculate $g_{mn}(\nu\mathbf{q})$ using the converged meshes. The grids are denoted as $N_1 \times N_2 \times N_3$ where N_i is the number of equisized intervals between lattice points along the reciprocal lattice direction $\mathbf{b}_i$. We write $N_{1,\text{e}} \times N_{2,\text{e}} \times N_{3,\text{e}}@\mathbf{k}$ for electronic and $N_{1,\text{p}} \times N_{2,\text{p}} \times N_{3,\text{p}}@\mathbf{q}$ for phonon grids. The electronic and phonon grids have to be commensurable $N_{i,\text{e}}/N_{i,\text{p}} \in \mathbb{N}$ within the DFPT implementation of **`exciting`** [35]. We use the generalized-gradient approximation to the exchange-correlation energy put forward by Perdew, Burke, and Ernzerhof (PBE) [36] for all our DFT and DFPT calculations.

For the construction of Wannier functions, we choose a large energy window such that $\epsilon_{\text{low}} \ll \pm\omega_{\text{D}} \ll \epsilon_{\text{up}}$. We then construct maximally localized WFs for that window and apply the transformations in Eqs. (2.70-2.72) and back transformations in Eqs. (2.73-2.75), to interpolate $h_{mn}(\mathbf{k})$, $D_{\nu\nu'}(\mathbf{q})$, and $g_{mn\nu}(\mathbf{k}, \mathbf{q})$ to denser $\mathbf{k}$ and $\mathbf{q}$ meshes. Then, we calculate the Eliashberg spectral function and the electron-phonon interaction function, Eqs. (2.23) and (2.24), with a

high resolution in $\mathbf{k}$ and $\mathbf{q}$ in an energy window of order $\sim\omega_{\mathrm{D}}$ around ϵ_{F}.

The Eliashberg equations, Eqs. (2.27) and (2.28), are then solved for MgB_2 for a set of temperatures, with a resolution of $\Delta T = 1\,\mathrm{K}$ around T_{c}. The value of T_{c} lies between the two temperature values, where the gap function goes from zero to nonzero values as the temperature decreases. While using Eqs. (2.27) and (2.28), we have to provide a value for μ^*. In the literature, μ^* is often treated as an adjustable parameter [10, 13], making it hard to directly compare T_{c} between calculations. For our calculations, we use the *ab initio* values of μ^* calculated by Moon and coworkers [20], leaving our workflow without any freely adjustable parameter thus making it able to directly predict the critical temperature T_{c}. For convergence tests regarding the self-consistent solution of Eqs. (2.27) and (2.28), we use the T_{c} calculated from the isotropic quantities in Eqs. (2.25) and (2.26). The software packages used in this work are described briefly in the following subsections.

3.1.1 `exciting`

The **`exciting`** package is used to solve Eqs. (2.43-2.46) for the entire electronic system of core and valence electrons. In **`exciting`** the unit cell of the crystal is separated into an interstitial and a muffin-tin region. This allows the use of a flexible basis set of augmented plane waves and local orbitals for the Hilbert space of Kohn-Sham (KS) wave functions [23]. The solution of Eqs. (2.43-2.46) is done in a self-consistent cycle up to convergence. For phonon calculations, the result of the converged KS system can be used to solve the Sternheimer equation 2.59 also in a self-consistent cycle [35].

Maximally localized Wannier Functions are calculated in **`exciting`** by iteratively decreasing the spread in Eq. (2.64) with respect to the unitary and semiunitary transformations in Eq. (2.66). A good starting point for this minimization is obtained using local orbitals [33].

3.1.2 `elphbolt`

In this work we use the **`superconda`** application of **`elphbolt`**, to handle the necessary calculations within the Eliashberg theory. The **`elphbolt`** package reads in the Wannier representations of the Hamiltonian, dynamical matrix and electron-phonon vertices and performs the transformations to arbitrary meshes in reciprocal space given in Eqs. (2.73-2.75). Using the imaginary time frame as described in Chapter 2, **`elphbolt`** computes the quantities in

Eqs. (2.23) and (2.24) [24] and then iteratively solves Eqs. (2.27) and (2.28) up to convergence for a given set of temperatures and performs the necessary analytic continuation.

3.2 Diamond under uniform strain

As a test for the implementation of our workflow, we compute $\alpha^2F(\omega)$ and λ for doped diamond under uniform strain, as all Wannier-interpolated quantities that we calculate are used within this computation. Diamond is an insulator that becomes metallic and shows superconductivity if it is hole doped [37]. To simulate doping, we apply a rigid shift to the Fermi level, choosing a chemical potential to obtain a carrier concentration equaling a B doping of 1.85%. This is the same doping level as in [31]. The structure of diamond is a face-centered cubic lattice with a basis of two carbon atoms. In our calculations, we get an equilibrium volume of $\Omega_0 = 45.614\,\text{Å}^3$. We use the 12×12×12@**k** and 6×6×6@**q** coarse grids for calculations for the pure diamond crystal. For the interpolated grids, we use 30×30×30@**k** and 30×30×30@**q**.

Figure 3.2 shows how the electronic band-structure (BS) and density of states (DOS) of diamond change under uniform volume strain. The phonon dispersion of diamond can be seen in Fig. 3.3. The electron-phonon interaction in doped diamond is dominated by the optical branches, as it can be seen in Fig. 3.4 that the Eliashberg spectral function $\alpha^2F(\omega)$ is very small in the acoustic compared to in the optical-energy region. We show the isotropic coupling strength λ from Eq. (2.26) in Fig. 3.5. Here λ decreases with decreasing volume of the unit cell. As already seen in the spectral function, the contributions to λ from optical and acoustic phonon branches behave differently with respect to the variation of the unit cell volume, Ω. The optical contribution to λ decreases with decreasing Ω and the acoustic contribution, which is relatively small, increases. For the relaxed system, we obtain $\lambda = 0.23$.

Our results can be compared to the work from Giustino and coworkers [31] who obtain $\lambda = 0.21$-0.23. The equilibrium volume is slightly different between the studies, which is explained by the different exchange and correlation potentials used. Comparing the Eliashberg spectral function $\alpha^2F(\omega)$ we can also see a qualitative difference that comes from the different treatment of doping, as we used a rigid band shift and they used the virtual-crystal approximation. This study makes us confident about the correctness of our methods.

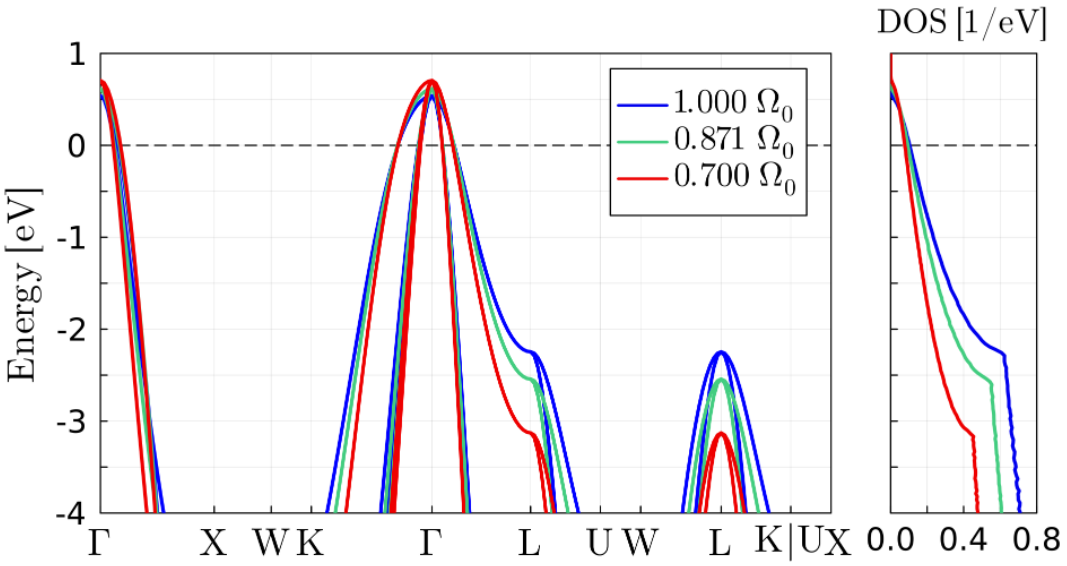

Figure 3.2: Electronic band structure and density of states for diamond at various volume strains. For each volume strain, the energy doped ϵ_F is set to be 0.

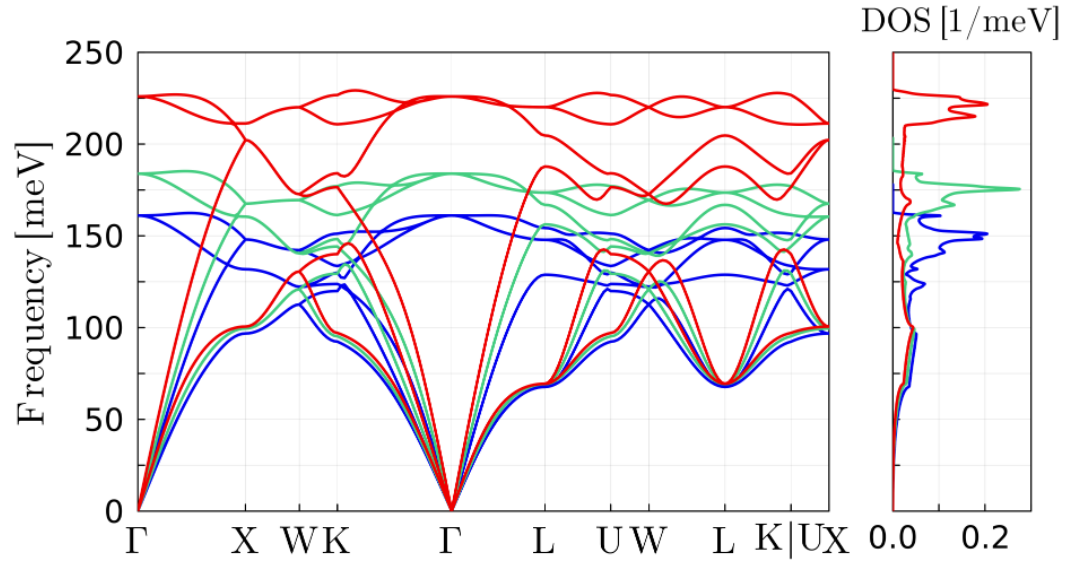

Figure 3.3: Phonon-dispersion curves and density of states for different volume strains of diamon. With volumes Ω_0 (equilibrium, blue lines), $0.871\,\Omega_0$ (green) and $0.700\,\Omega_0$ (red).

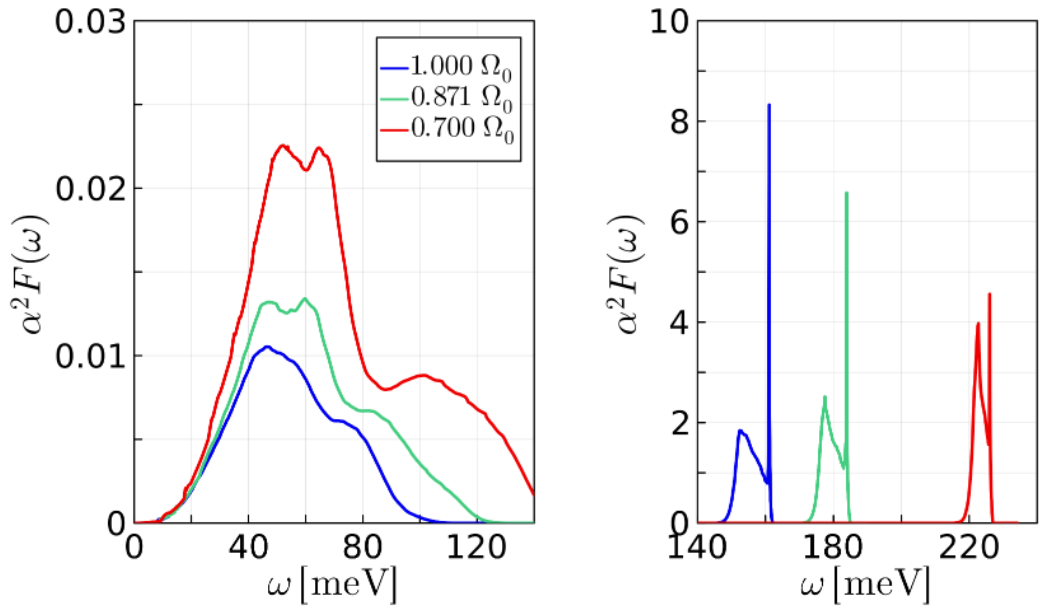

Figure 3.4: Isotropic spectral function, $\alpha^2F(\omega)$, of diamond under volume strain, for the acoustic (left panel) and optical (right panel) energy range. Notice also the different scale of the spectral function in the two panels.

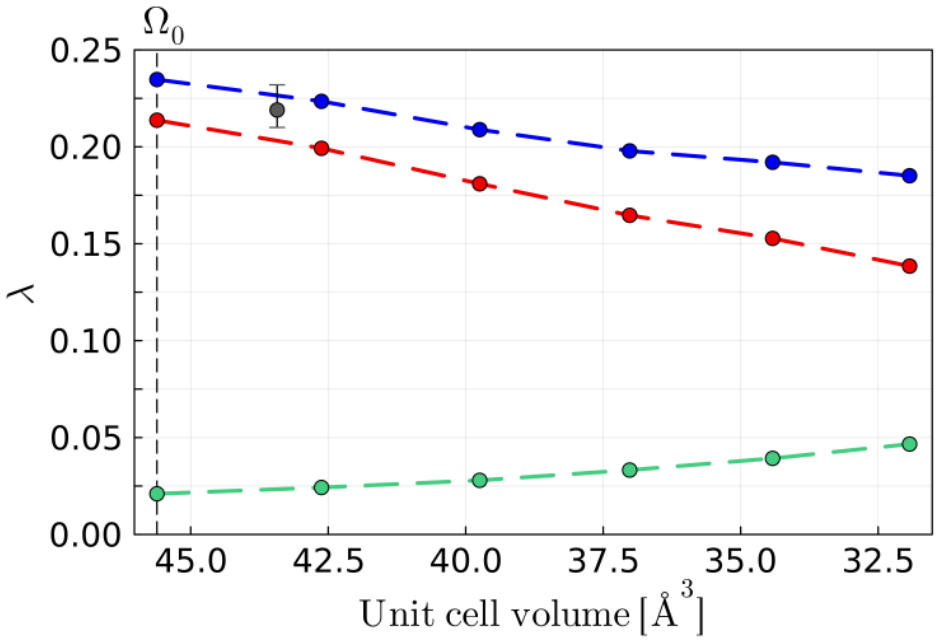

Figure 3.5: Electron-phonon-coupling strength λ as a function of the volume: Full value (blue), optic contribution (red), and acoustic contribution (green). The value obtained by Giustino and coworkers [31] is also shown for comparison (grey).

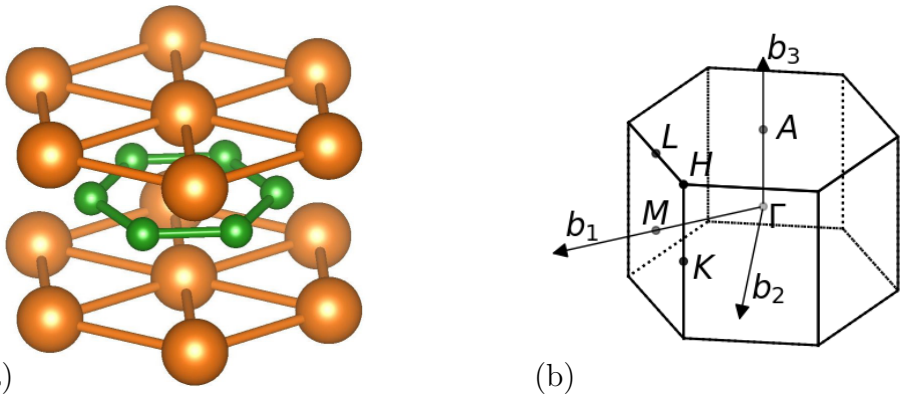

(a) (b)

Figure 3.6: (a) Crystal structure of MgB_2 with Mg (orange) and B (green) atoms. (b) First Brillouin zone of MgB_2, with reciprocal lattice vectors $\{\mathbf{b}_i\}$.

3.3 Magnesium diboride

Having presented and tested our methods, we now show our results for MgB_2. We obtain these results using coarse grids of $24\times24\times21@\mathbf{k}$ and $8\times8\times7@\mathbf{q}$. The Wannier-interpolated grids are $40\times40\times35@\mathbf{k}$ and $40\times40\times35@\mathbf{q}$.

3.3.1 Crystal, electronic, and phonon structure

The crystal structure and first Brillouin zone of MgB_2 can be seen in Fig. 3.6. The material consists of alternating Mg and B layers that are hexagonally stacked and the lattice vectors can be given in the form $\mathbf{a}_1 = a\,\vec{e}_1$, $\mathbf{a}_2 = a\,\vec{e}_2$, and $\mathbf{a}_3 = c\,\vec{e}_3$ with the unit vectors

$$\vec{e}_{1,2} = \frac{1}{2}\begin{pmatrix}1 & \pm\sqrt{3} & 0\end{pmatrix}^{\mathrm{T}}, \qquad \vec{e}_3 = \begin{pmatrix}0 & 0 & 1\end{pmatrix}^{\mathrm{T}}. \tag{3.1}$$

For the equilibrium structure we obtain the lattice constants of $a = 0.3077\,\mathrm{nm}$, $c = 0.3523\,\mathrm{nm}$, and their ratio $c/a = 1.145$. These values are in very good agreement with the experimentally measured result of $a = 0.3086\,\mathrm{nm}$ and $c = 0.3524\,\mathrm{nm}$ [38].

The electronic band-structure (BS) of the material obtained from the back transformation of the Wannier functions (WF), Eq. (2.73), can be seen in Fig. 3.7. Our WFs, of which we show two in Fig. 3.8, can be distinguished into in and out of plane functions, similar to in plane σ- and out of plane π-bonds

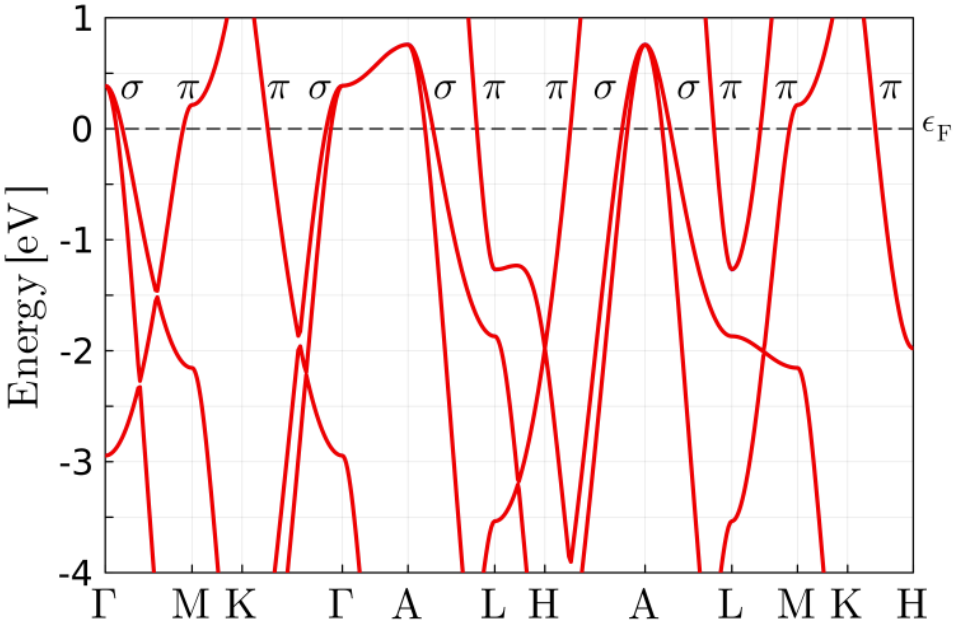

Figure 3.7: Electronic band structure of MgB_2. The bands are labeled by either σ or π, depending on their composition of WFs at ϵ_F .

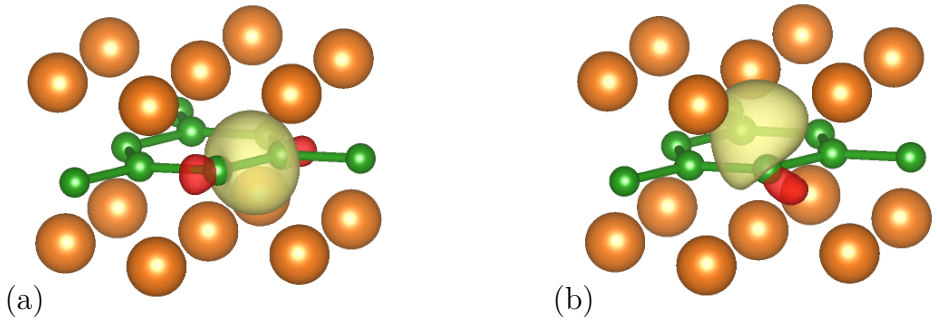

Figure 3.8: (a) σ-like Wannier function of MgB_2 . (b) π-like Wannier function.

within the Boron layers of the crystal. Using this classification, we can see from the absolute squared of the matrix elements in Eq. (2.67) which WFs are dominant in the construction of what bands. This allows us to label the bands at the Fermi surface to be of either σ or π character, depending on the weight of the WFs from which they are constructed.

Table 3.1: $E_{2g}(\Gamma)$ and $E_{2g}(A)$ phonon energies of MgB_2, for different **k** and **q** grids. Energies are given in meV.

grid@**k**	grid@**q**	$E_{2g}(\Gamma)$	$E_{2g}(A)$
12×12×10	6×6×5	68.63	64.87
16×16×14	8×8×7	71.63	69.51
18×18×15	6×6×5	71.52	63.95
24×24×20	6×6×5	71.18	65.24
24×24×21	8×8×7	71.07	64.52

In Table 3.1 we show our values for the energy of the $E_{2g}(\Gamma)$ and $E_{2g}(A)$ phonon modes,[1] for different grids. The grids are chosen such that

$$\frac{N_1}{N_3} \approx \frac{|\mathbf{b}_1|}{|\mathbf{b}_3|} = \frac{c}{a}\,. \tag{3.2}$$

These E_{2g} phonon modes are the most sensitive modes with respect to the reciprocal lattice grids. This shows how the phonon dispersion of MgB_2 converges relatively slow with respect to the electronic **k**-grid. By comparing the phonon dispersion, shown in Fig. 3.9, for the grids 6×6×5@**q** and 8×8×7@**q**, we can see a slight difference in $E_{2g}(\Gamma\text{-A})$ energy between the calculations. However this difference does not cause a relevant difference in λ, as can be seen in Table 3.2.

In Fig. 3.9, we can see that our phonon dispersion compares very well to different sets of experimental x-ray scattering data [39–41]. Significant differences can only be seen for the energy of $E_{2g}(\Gamma\text{-A})$ phonons, where our result is slightly above the experimental x-ray scattering data. However, different groups have performed Raman scattering experiments, which predict the energy of $E_{2g}(\Gamma)$ to be either 76 meV [42–44] or 71 meV [17]. The x-ray scattering data from Ref. [39] has a data point for the energy of $E_{2g}(\Gamma\text{-A})$, that is relatively close to Γ, which allows us to estimate their $E_{2g}(\Gamma)$ energy to be approximately 68 meV using a quadratic fit centered at Γ. This value is significantly lower than the $E_{2g}(\Gamma)$ energies measured by Raman scattering [17, 39–41]. Our calculated value of about 71 meV lies in between the different experimental values.

Comparing our DOS to the work of Margine and coworkers [45], we can see

[1] In the Γ-A direction, the E_{2g} phonon modes have branch index $\nu = 7, 8$. Their eigenvectors can be seen in Fig. 3.10.

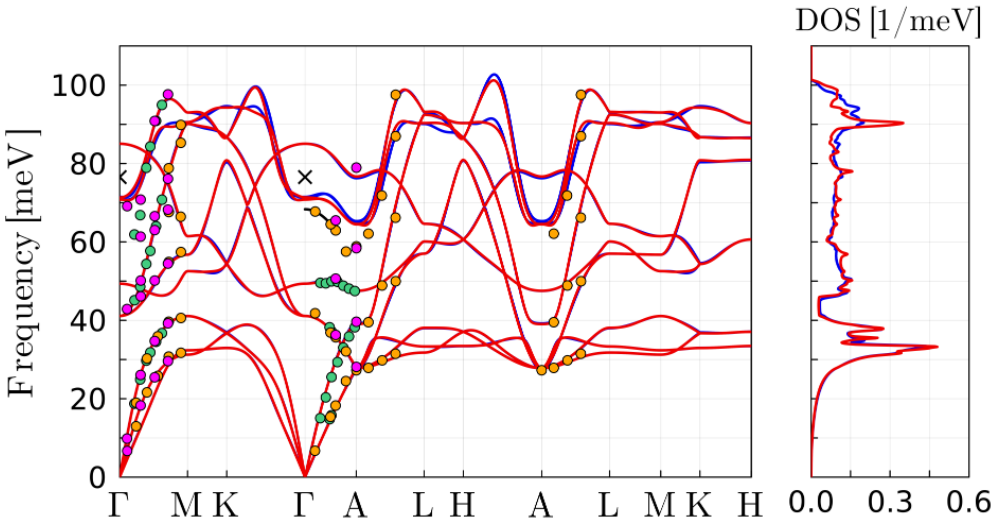

Figure 3.9: Phonon dispersion curves and density of states of MgB_2 from Wannier interpolation for 24×24×20@**k**, 6×6×5@**q** (blue) and 24×24×21@**k**, 8×8×7@**q** (red). We compare our dispersion with different x-ray scattering data (orange) [39], (green) [40], and (pink) [41] as well as Raman-scattering data (crosses) [42].

that the two densities are in very good agreement. The difference in E_{2g}(Γ-A) energy is, nevertheless, visible when comparing the shape of the DOS in the range between 55 and 70 meV.

3.3.2 Electron-phonon interaction

In the last section, we presented the band structure of electrons and phonons in MgB_2. These properties give rise to the complicated nature of electron-phonon interaction in MgB_2. The eigenvectors of E_{2g} phonons shown in Fig. 3.10 are in-plane displacements of the boron atoms. The perturbation due to the external potential from these displacements has a strong impact on σ-bonds and a weak impact on π-bonds within the Boron layers. Thus, the σ-like bands at the Fermi surface couple very strongly to these phonons and conversely, the coupling of the π-like bands to E_{2g} phonons is relatively weak [46]. In order to capture these features, we have to treat the material using the anisotropic as well as band and branch-resolved Eliashberg theory (ET) described in Chapter 2.3. The difference in electron-phonon-coupling between σ and π-like bands also gives rise to the two-gap structure of $\Delta_{n\mathbf{k}}^{(\mathrm{F})}$, seen in Fig. 3.14 within the

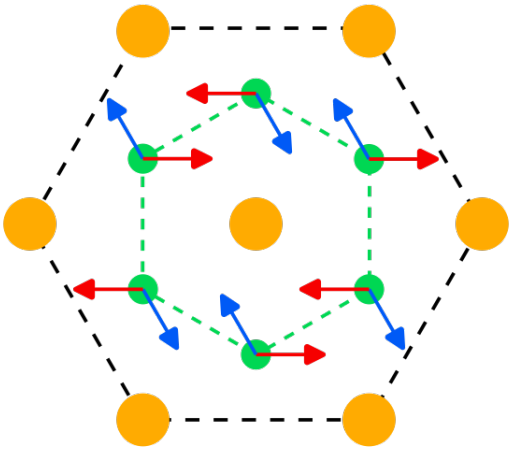

Figure 3.10: Phonon eigenvectors of the two degenerate $E_{2g}(\Gamma)$ phonon mode (red,blue) of MgB_2 with Mg (orange) and B (green).

next section. This figure also shows the drastic difference in T_c comparing the anisotropic to the isotropic ET.

We show the calculated isotropic spectral function $\alpha^2F(\omega)$ and the accumulation of λ in Fig. 3.11. The contribution of $E_{2g}(\Gamma\text{-A})$ phonons is given by $\alpha^2F_{\nu=7}(\omega)$ and $\alpha^2F_{\nu=8}(\omega)$ in the energy range of about 63 to 71 meV and it is depicted that these phonon branches give the largest contribution to the electron-phonon interaction. Comparing to the work of Margine and coworkers [13], we can see that their λ is higher and their $E_{2g}(\Gamma)$ energy is lower than ours. From the accumulation of λ it is apparent that the differences in λ arise from the contribution of the $E_{2g}(\Gamma\text{-A})$ phonons.

As already mentioned, there are many first-principles studies of electron-phonon interaction in MgB_2. In Table 3.2, we compare λ and the $E_{2g}(\Gamma)$ energies with previous investigations. It can be seen that the $E_{2g}(\Gamma)$ energy is usually lower for calculations that use experimental lattice constants, compared to calculations using the DFT equilibrium structure. A further important observation from Table 3.2 is that calculations using the relaxed crystal structure and the PBE functional obtain an $E_{2g}(\Gamma)$ energy of around 70 meV and a λ of around 0.63 . The ratio of λ and the $E_{2g}(\Gamma)$ energy is displayed in Fig. 3.12. From this we can see a direct connection between λ and the $E_{2g}(\Gamma)$ energy, with our results being in very good agreement with the trend line.

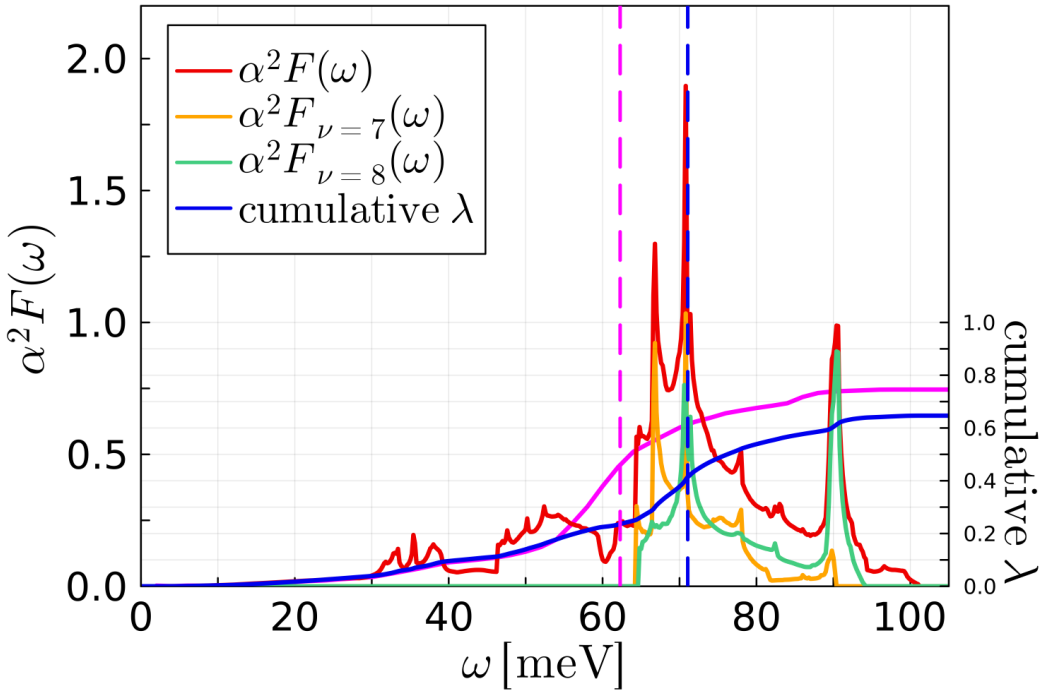

Figure 3.11: Isotropic spectral function $\alpha^2F(\omega)$ and accumulation of λ in MgB_2 in comparison with the results of Margine and coworkers [13] (pink lines). The vertical dashed lines indicate the $E_{2g}(\Gamma)$ energies of the calculations identified by the same color.

Table 3.2: electron-phonon-coupling strength λ and $E_{2g}(\Gamma)$ energy (in units of meV) for different *ab initio* calculations with coarse grids @**k** and @**q**. The second column give the color code in Fig. 3.12.

	color	$E_{2g}(\Gamma)$	λ	@**k**	@**q**	v_{xc}
$\Omega_{exp.}$						
Ref. [15]	pink	66.31	0.776	20^3	10^3	-
Ref. [13]	green	62.28	0.75	24^3	6^3	LDA
Ref. [34]	purple	67	0.68	12^3	6^3	LDA
Ref. [12]	orange	65.11	0.741	$16^2\times12$	$6^2\times4$	-
Ref. [16]	black	72.53	0.87	$12^2\times6$	6^3	LDA
Ω_0 DFT						
Ref. [10]	red	62.66	0.73	12^3	**	LDA
Ref. [10]*	red	75.86	0.61	12^3	**	LDA
Ref. [17]	yellow	70.75	0.73	-	6^3	LDA
Ref. [18]	white	70.22	0.643	12^3	6^3	PBE
Ref. [19]	teal	67.15	0.62	-	-	PBE
This work	blue	71.48	0.63	$24^2\times20$	$6^2\times5$	PBE
This work	blue	71.07	0.65	$24^2\times21$	$8^2\times7$	PBE

(*) Anharmonic phonon energies.
(**) Phonons calculated only at high-symmetry points.

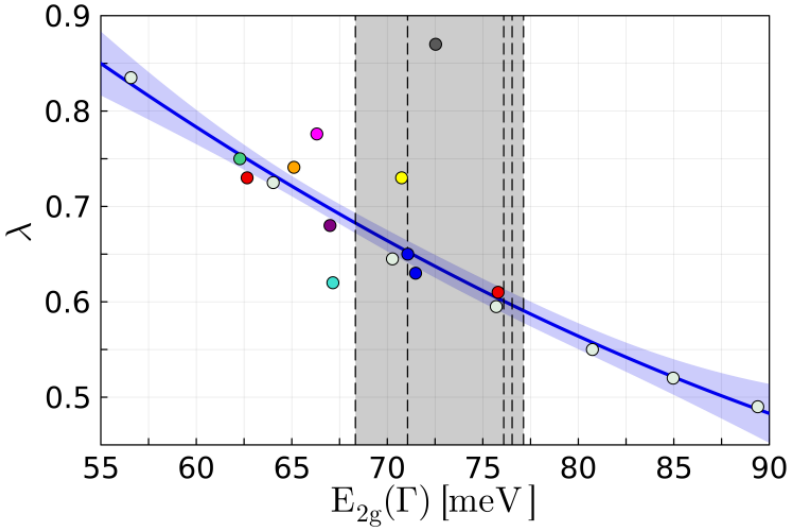

Figure 3.12: The ratio of λ and $E_{2g}(\Gamma)$ energy for the values from Table 3.2. The dashed lines are the experimental values, with the lowest energy being the estimate from x-ray scattering data and the other being the Raman scattering values [17, 42–44].

3.3.3 Superconductivity

Capturing electron-phonon interaction correctly is very important for a theoretical study of conventional superconductors. Our results for the electron-phonon-coupling strength λ, which gives a measure for the electron-phonon-interaction function, Eq. (2.24), are presented in the previous section. We can see a connection between the $E_{2g}(\Gamma)$ energy and λ.

In order to solve Eqs. (2.27) and (2.28) and determine the critical temperature T_c, we have to choose a value for μ^*. An *ab initio* investigation of μ^* within MgB_2 has been conducted by Moon and coworkers [20], they calculate this parameter using the full dielectric matrix and obtain $\mu^* = 0.118$ using the Debye energy ω_D as a cut-off and $\mu^* = 0.151$ for a cut-off of $0.5\,\text{eV} \approx 5\,\omega_D$. In our calculations, we used a phonon cut-off of $6\,\omega_D$ and we obtain a $T_c = 37\,\text{K}$ for $\mu^* = 0.118$ and $T_c = 33.5\,\text{K}$ for $\mu^* = 0.151$. Both of these results are close to the experimentally measured T_c of 39 K [38], which shows that our calculations give a good prediction of T_c within a reasonable range of μ^*.

In the superconducting phase, there is a gap in the electronic quasi-particle density of states (DOS). The temperature dependence of this DOS is shown in Fig. 3.13. It can be seen that the DOS discontinuously changes between $T = 38\,\text{K}$ and $T = 36\,\text{K}$ which signifies the phase transition between the normal and the superconducting state at about $T = 37\,\text{K}$. Comparing the DOS of the isotropic and anisotropic ET for $T = 5\,\text{K}$, we can see that the anisotropic DOS has a structure of two gaps, a large gap for the σ and a smaller gap for the π-bands at the Fermi surface. We plot the distribution of $\Delta_{n\mathbf{k}}^{(F)}$ in Fig. 3.14, where this two-gap structure is also visible as there are two separate clusters of $\Delta_{n\mathbf{k}}^{(F)}$ values.

The only existing works, that have studied superconductivity in MgB_2 within the anisotropic Eliashberg theory are the works of Choi and coworkers [10] and Margine and coworkers [13]. We can see, that the values of λ and $E_{2g}(\Gamma)$ energy of these works and our work are consistent with the expected ratio seen in Fig. 3.12. We also note, that our result for the $E_{2g}(\Gamma)$ energy and the anharmonic $E_{2g}(\Gamma)$ energy from Ref. [10] are within the range of experimental values. A study conducted by Lazzeri and coworkers [11] has demonstrated that three and four-phonon corrections to the $E_{2g}(\Gamma\text{-A})$ energies mostly cancel in MgB_2, suggesting that the bare phonons, as we calculated them, should give good results for the energies of $E_{2g}(\Gamma\text{-A})$.

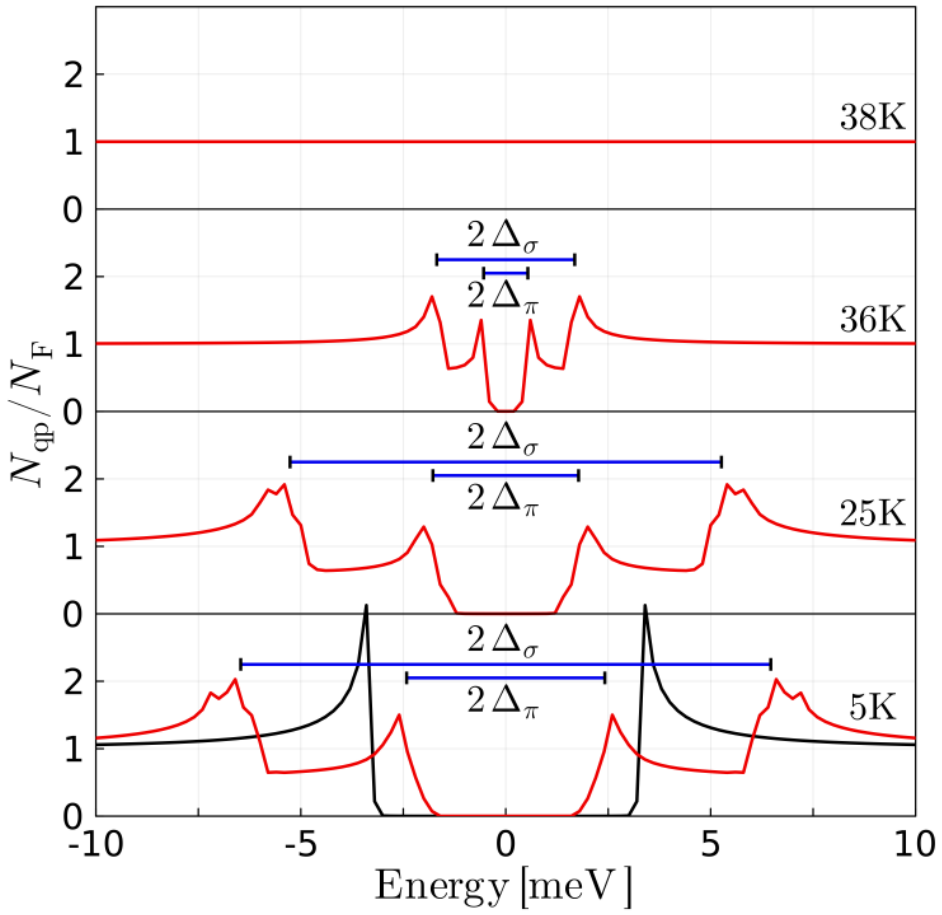

Figure 3.13: Electronic quasi-particle density of states ($N_{\mathrm{qp}}(\omega)$). Δ_σ and Δ_π are acquired from BCS like fits, shown in Fig. 3.14. The quasi-particle density of states for the isotropic theory is shown in black.

The T_{c} of 37 K and the two gap values at $T = 0\,\mathrm{K}$ of $\Delta_\sigma = 6.5\,\mathrm{meV}$ and $\Delta_\pi = 2.4\,\mathrm{meV}$ that we report for $\mu^* = 0.118$ are in good agreement with the results from anharmonic phonons in Ref. [10]. We compare our electron-phonon interaction with the work from Ref. [13] in Fig. 3.11 and we mentioned in the previous section, that any difference can be attributed to the $\mathrm{E}_{2\mathrm{g}}(\Gamma\text{-A})$ phonons. This observation is validated by the comparison of both Δ_π and Δ_σ between the calculations. The values of Δ_π are in good agreement, as Δ_π is not significantly affected by the energy of $\mathrm{E}_{2\mathrm{g}}(\Gamma\text{-A})$ phonons. For Δ_σ we can see that their value of $\Delta_\sigma \approx 8.5, \mathrm{meV}$ is significantly larger than ours. Their strong electron-phonon interaction, together with $\mu^* = 0.16$.

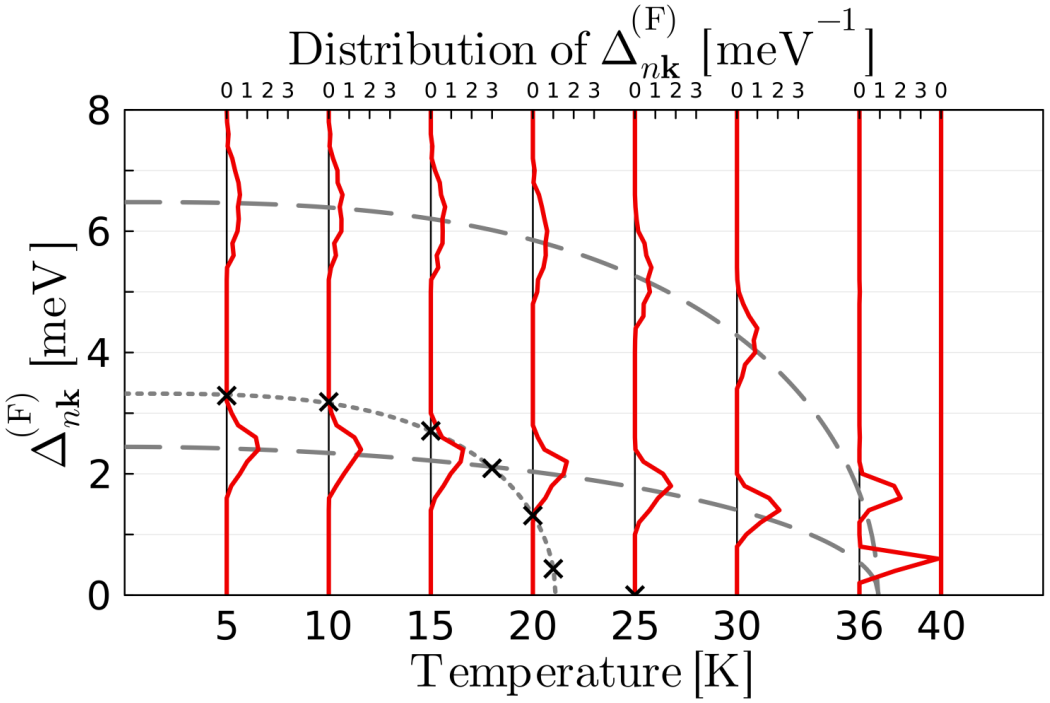

Figure 3.14: Distribution of $\Delta^{(\mathrm{F})}_{n\mathbf{k}}$ for $\mu^* = 0.118$ (red) and the isotropic approximation (black crosses). The dashed lines are the two gap values $\Delta_\sigma(T)$ and $\Delta_\pi(T)$, fitted using a BCS-like fit $\Delta_{\sigma/\pi}(T) = \Delta_{\sigma/\pi}\left[1 - (T/T_\mathrm{c})^p)\right]^{1/2}$ [46]. $\Delta^{(\mathrm{F})}_{n\mathbf{k}}$ vanishes at about 37 K.

Chapter 4

Conclusions and Outlook

In this work, we conducted an *ab initio* study of superconductivity in MgB_2 combining Eliashberg theory with methods based on density-functional theory, using and testing the new interface between the software packages **exciting** and **elphbolt**. We tested our methods using pressurized diamond, confirming the functionality of newly implemented features within both codes.

Our investigation suggests that Eliashberg theory (ET) is able to predict the critical temperature of MgB_2 reasonably well. The main difference between our work and the established results that used ET [10, 13] is that we obtain a lower electron-phonon coupling to the $E_{2g}(\Gamma\text{-A})$ phonons, which is reflected in our λ of 0.65 . This lower coupling strength manifests itself in a significantly more accurate prediction of the critical temperature T_c and gap for the σ bands Δ_σ .

From our structure relaxation, we get lattice constants that are in very good agreement with experimental values using the PBE exchange and correlation functional. For this structure, we obtain a phonon dispersion that is in good agreement with experimental data. For the energy of the $E_{2g}(\Gamma\text{-A})$ phonons, there is a discrepancy between x-ray and Raman scattering data, and our values lie between the results.

Comparing our calculation and other first-principles studies of the electron-phonon interaction in MgB_2 , we can see that relaxing the structure has a significant impact on the energy of the $E_{2g}(\Gamma\text{-A})$ phonon energies and that a better agreement with experimental results is obtained for the DFT equilibrium structure. This comparison also shows a clear connection between the energy of the $E_{2g}(\Gamma\text{-A})$ phonons and the electron-phonon-coupling strength.

Our work is unique in studying MgB_2 using the branch and band resolved ET, that is anisotropic in both $\mathbf{k}$ and $\mathbf{q}$, using a relaxed structure and the PBE exchange and correlation functional. We obtain a $T_c = 37\,\mathrm{K}$ using $\mu^* = 0.118$ and $T_c = 33.5\,\mathrm{K}$ for $\mu^* = 0.151$. Although we do not know, if the first-principles μ^* values from Ref. [20] are fully consistent with our calculations, it is apparent that the impact of μ^* on the T_c is small compared to the impact of the anisotropic treatment of electron-phonon interaction and the $E_{2g}(\Gamma\text{-A})$ energies.

In conclusion, our framework is able to describe superconductivity in MgB_2. Anisotropic treatment of the electron-phonon interaction is necessary for a qualitatively correct description of the material and the quality of T_c is affected mostly by the energy of $E_{2g}(\Gamma\text{-A})$ phonons, with a good T_c for $E_{2g}(\Gamma)$ values that are compatible with experimental data. Our calculations give a range of T_c between 33.5-37.0 K, depending on the value of μ^*. Stronger electron-phonon interaction, that results in a higher T_c, can be achieved for slightly lower $E_{2g}(\Gamma\text{-A})$ energies that are closer to the x-ray scattering data in Refs. [39–41].

Concerning the future continuation of our work, the first logical step to improve our results is to calculate μ^* ourselves, in order to reduce the range of reasonable T_c to a single value. Our investigation reveals, that the discrepancies between the existing studies of MgB_2 arise from the different values of the $E_{2g}(\Gamma\text{-A})$ energies that are calculated using DFT and DFPT. For this, we have already concluded, that the relaxation of the unit cell is important but the isolated effect of different exchange and correlation potentials should also be investigated.

Bibliography

[1] M. Tinkham and G. McKay. *Introduction to Superconductivity second edition*. Dover publications, 2004.

[2] A. Bussmann-Holder and H. Keller. "High-temperature superconductors: underlying physics and applications". In: *Z. Naturforsch. 2019* 75 (2019).

[3] K. Onnes. In: *Comm. Leiden* 120b-124c (1911).

[4] W. Meissner and R. Ochsenfeld. "Ein neuer Effekt bei Eintritt der Supraleitfähigkeit". In: *Naturwissenschaften* 21 787-788 (1933).

[5] J. Bardeen, L. N. Cooper, and J. R. Schrieffer. "Theory of Superconductivity". In: *Phys. Rev.* 108 1175 (1957).

[6] H. K. Bennemann and J. B. Ketterson. *Superconductivity Conventional and Unconventional Superconductors*. Springer-Verlag Berlin Heidelberg, 2008.

[7] J. G. Bednorz and K. A. Müller. "Possible High T_c Superconductivity in the Ba-La-Cu-O System". In: *Z. Phys. B Cond. Mat.* 64 189-193 (1986).

[8] J. Nagamatsu, N. Nakagawa, T. Muranaka, and Y. Zenitani J. Akimitsu. "Superconductivity at 39K in magnesium diboride". In: *Nature* 410 63–64 (2001).

[9] S. L. Bud'ko, G. Lapertot, C. Petrovic, C. E. Cunningham, N. Anderson, and P. C. Canfield. "Boron Isotope Effect in Superconducting MgB_2". In: *Phys. Rev. Lett.* 86 1877 (2001).

[10] H. J. Choi, M. L. Cohen, and S. G. Louie. "Anisotropic Eliashberg theory of MgB_2 : T_c isotope effects, superconducting energy gaps, quasiparticles and specific heat". In: *Physica C: Superconductivity* 385 66-74 (2003).

[11] M. Lazzeri, M. Calandra, and F. Mauri. "Anharmonic phonon frequency shift in MgB_2". In: *Phys. Rev. B* 68 220509 (2003).

[12] M. Calandra, G. Profeta, and F. Mauri. "Adiabatic and nonadiabatic phonon dispersion in a Wannier function approach". In: *Phys. Rev. B* 82 165111 (2010).

[13] E. R. Margine and F. Giustino. "Anisotropic Migdal-Eliashberg theory using Wannier functions". In: *Phys. Rev. B* 87 024505 (2013).

[14] A. Floris, A. Sanna, M. Lüders, G. Profeta, N. N. Lathiotakis, M. A. L. Marques, C. Franchini, E. K. U. Gross, A. Continenza, and S. Massidda. "Superconducting Properties of MgB_2 from First Principles". In: *Physica C* 456 45-53 (2007).

[15] A. Eiguren and C. Draxl. "Wannier interpolation scheme for phonon-induced potentials: Application to bulk MgB_2 , W, and the (1×1) H-covered W(110) surface". In: *Phys. Rev. B* 78 045124 (2008).

[16] Y. Kong, O. V. Dolgov, O. Jepsen, and O. K. Andersen. "Electron-phonon interaction in the normal and superconducting states of MgB_2". In: *Phys. Rev. B* 64 020501 (2001).

[17] K. P. Bohnen, R. Heid, and B. Renker. "Phonon Dispersion and Electron-Phonon Coupling in MgB_2 and AlB_2". In: *Phys. Rev. Lett.* 86 5771 (2001).

[18] E. Johansson, F. Tasnádi, A. Ektarawong, J. Rosen, and B. Alling. "The effect of strain and pressure on the electron-phonon coupling and superconductivity in MgB_2—Benchmark of theoretical methodologies and outlook for nanostructure design". In: *J. Appl. Phys.* 131 063902 (2022).

[19] N. Girotto and D. Novko. "Dynamical renormalization of electron-phonon coupling in conventional superconductors". In: *Phys. Rev. B* 107 064310 (2023).

[20] C. Y. Moon, Y. H. Kim, and K. J. Chang. "Dielectric-screening properties and Coulomb pseudopotential μ^* for MgB2". In: *Phys. Rev. B* 70 104522 (2004).

[21] P. Hohenberg and W. Kohn. "Inhomogeneous Electron Gas*". In: *Phys. Rev. B* 136 B864 (1964).

[22] X. Gonze and J. P. Vigneron. "Density-functional approach to nonlinear-response coefficients of solids". In: *Phys. Rev. B* 39 13120 (1988).

[23] A. Gulans, S. Kontur, C. Meisenbichler, D. Nabok, P. Pavone, S. Rigamonti, S. Sagmeister, U. Werner, and C. Draxl. "exciting: a full-potential all-electron package implementing density-functional theory and many-body perturbation theory". In: *J. Phys.: Condensed Matter* 26 363202 (2024).

[24] N. H. Protik, C. Li, M. Pruneda1, D. Broido, and P. Ordejón. "The elphbolt ab initio solver for the coupled electron-phonon Boltzmann transport equations". In: *npj Comput Mater* 8 28 (2022).

[25] H. Bruus and K. Flensberg. *Many-Body Quantum Theory in Condensed Matter Physics : An Introduction*. Oxford University Press, Incorporated, 2004.

[26] R. A. Jishi. *Feynman Diagram Techniques in Condensed Matter Physics*. Cambridge University Press, 2013.

[27] P. Morel and P. W. Anderson. "Calculation of the Superconducting State Parameters with Retarded Electron-Phonon Interaction". In: *Phys. Rev. B* 125 1263 (1962).

[28] H. J. Vidberg and J. W. Serene. "Solving the Eliashberg Equations by Means of N-Point Pade Approximants". In: *J. Phys.: Low Temperature Physics* 29 (1977).

[29] W. Kohn and L. J. Sham. "Self-Consistent Equations Including Exchange and Correlation Effects*". In: *Phys. Rev.* 140 A1133 (1965).

[30] X. Gonze and C. Lee. "Dynamical matrices, Born effective charges, dielectric permittivity tensors, and interatomic force constants from density-functional perturbation theory". In: *Phys. Rev. B* 55 10355 (1997).

[31] F. Giustino, M. L. Cohen, and S. G. Louie. "Electron-phonon interaction using Wannier functions". In: *Phys. Rev. B* 76 165108 (2007).

[32] I. Souza, N. Marzari, and D. Vanderbilt. "Maximally localized Wannier functions for entangled energy bands". In: *Phys. Rev. B* 65 035109 (2001).

[33] S. Tillack, A. Gulans, and C. Draxl. "Maximally localized Wannier functions within the (L)APW + LO method". In: *Phys. Rev. B* 101 235102 (2020).

[34] P. P. Singh. "From E_{2g} to Other Modes: Effects of Pressure on Electron-Phonon Interaction in MgB_2". In: *Phys. Rev. Lett.* 97 247002 (2006).

[35] S. Tillack, P. Pavone, and C. Draxl. To be published.

[36] J. P. Perdew, K. Burke, and M. Ernzerhof. "Generalized Gradient Approximation Made Simple". In: *Phys. Rev. Lett.* 77 3865 (1996).

[37] V. A. Sidorov, E. A. Ekimova, E. D. Bauer, N. N. Mel'nik, N. J. Curro, V. Fritsch, J. D. Thompson, S. M. Stishov, A. E. Alexenko, and B.V. Spitsyn. "Superconductivity in boron-doped diamond". In: *Diamond and Related Materials* 14 335-339 (2005).

[38] J. Nagamatsu, N. Nakagawa, T. Muranaka, Y. Zenitani, and J. Akimitsu. "Superconductivity at 39 K in magnesium diboride". In: *Nature* 410 63-64 (2001).

[39] A. Shukla, M. Calandra, M. d'Astuto, M. Lazzeri, F. Mauri, C. Bellin, M. Krisch, J. Karpinski, S. M. Kazakov, J. Jun, D. Daghero, and K. Parlinski. "Phonon Dispersion and Lifetimes in MgB_2". In: *Phys. Rev. Lett.* 90 095506 (2003).

[40] A. Q. R. Baron, H. Uchiyama, S. Tsutsui, Y. Tanaka, D. Ishikawa, J. P. Sutter, S. Lee, S. Tajima, R. Heid, and K. P. Bohnen. "Phonon spectra in pure and carbon doped MgB 2 by inelastic X-ray scattering". In: *Physica C* 456 83-91 (2007).

[41] M. d'Astuto, M. Calandra, S. Reich, A. Shukla, M. Lazzeri, F. Mauri, J. Karpinski, N. D. Zhigadlo, A. Bossak, and M. Krisch. "Weak anharmonic effects in MgB_2: A comparative inelastic x-ray scattering and Raman study". In: *Phys. Rev. B* 75 174508 (2007).

[42] J. W. Quilty, S. Lee, A. Yamamoto, and S. Tajima. "Superconducting Gap in MgB 2: Electronic Raman Scattering Measurements of Single Crystals". In: *Phys. Rev. Lett.* 88 087001 (2002).

[43] J. Hlinka, I. Gregora, J. Pokorný, A. Plecenik, P. Kúš, L. Satrapinsky, and Š. Beňačka. "Phonons in MgB_2 by polarized Raman scattering on single crystals". In: *Phys. Rev. B* 64 140503 (2001).

[44] A. F. Goncharov, V. V. Struzhkin, E. Gregoryanz, J. Hu, R. J. Hemley, H. Mao, G. Lapertot, S. L. Bud'ko, and P. C. Canfield. "Raman spectrum and lattice parameters of MgB_2 as a function of pressure". In: *Phys. Rev. B* 64 100509 (2001).

[45] S. Poncé, E. R. Margine, C. Verdi, and F. Giustino. "EPW: Electron-phonon coupling, transport and superconducting properties using maximally localized Wannier functions". In: *Comp. Phys. Com.* 209 116-133 (2016).

[46] H. J. Choi, D. Roundy, H. Sun, M. L. Cohen, and S. G. Louie. "The origin of the anomalous superconducting properties of MgB_2". In: *Nature* 418 758–760 (2002).

Selbstständigkeitserklärung

Ich erkläre hiermit, dass ich die vorliegende Arbeit selbstständig verfasst und noch nicht für andere Prüfungen eingereicht habe. Sämtliche Quellen einschließlich Internetquellen, die unverändert oder abgewandelt wiedergegeben werden, insbesondere Quellen für Texte, Grafiken, Tabellen, Bilder sowie die Nutzung von Künstlicher Intelligenz für die Erstellung von Texten und Abbildungen, sind als solche kenntlich gemacht. Mir ist bekannt, dass bei Verstößen gegen diese Grundsätze ein Verfahren wegen Täuschungsversuchs bzw. Täuschung eingeleitet wird.

Berlin, _____